

Development of contact algorithm for three-dimensional numerical manifold method

L. He, X.M. An and Z.Y. Zhao*,†

School of Civil and Environmental Engineering, Nanyang Technological University, Singapore, 639798

SUMMARY

This paper customizes a contact detection and enforcing scheme to fit the three-dimensional (3-D) numerical manifold method (NMM). A hierarchical contact system is established for efficient contact detection. The mathematical mesh, a unique component in the NMM, is utilized for global searching of possible contact blocks and elements, followed by the local searching to identify primitive hierarchies. All the potential contact pairs are then transformed into one of the two essential entrance modes: point-to-plane and crossing-lines modes, among which real contact pairs are detected through a unified formula. The penalty method is selected to enforce the contact constraints, and a general contact solution procedure in the 3-D NMM is established. Because of the implicit framework, an open-close iteration is performed within each time step to determine the correct number of contact pairs among multi-bodies and to achieve complete convergence of imposed contact force at corresponding position. The proposed contact algorithm extensively utilizes most of the original components of the NMM, namely, the mathematical mesh/cells and the manifold elements, as well as the external components associated with contacts, such as the contact body, the contact facet and the contact vertex. In particular, the utilization of two mutually approaching mathematical cells is efficient in detecting contacting territory, which makes this method particularly effective for both convex and non-convex bodies. The validity and accuracy of the proposed contact algorithm are verified and demonstrated through three benchmark problems. Copyright © 2013 John Wiley & Sons, Ltd.

Received 27 August 2012; Revised 15 May 2013; Accepted 1 October 2013

KEY WORDS: three-dimensional numerical manifold method; contact detection; contact enforcement

1. INTRODUCTION

Since its initiation in 1991 [1], the two-dimensional (2-D) numerical manifold method (NMM) has been extensively studied and utilized in various engineering studies and applications [2–12], and has shown its outstanding capabilities in the following aspects: (1) *convenient pre-processing* – a regular mesh is always applicable regardless of the complexity of the problem domain; (2) *efficient discontinuity modeling* – discontinuities are modeled in a natural manner by its dual cover system, with neither mesh conforming to discontinuities nor remeshing for discontinuity evolution; and (3) *capability of describing combined continuum-discontinuum problems* – the NMM combines the continuum-based FEM and discontinuum-based discontinuous deformation analysis (DDA) [13–18] within a single framework. As a hybrid continuum-discontinuum method, the NMM can accurately describe the displacement/stress field within each block by employing a set of covers, separation and sliding along existing discontinuities, fracturing of intact rock and post-failure movement of discrete blocks. Recently, the NMM has also been extended to three-dimensional (3-D) domain. Continuous

*Correspondence to: Z.Y. Zhao, School of Civil and Environmental Engineering, Nanyang Technological University, Singapore, 639798.

†E-mail: czzhao@ntu.edu.sg

version of 3-D NMM has been developed in [19–22]. Basic formulation of the 3-D NMM together with a preliminary contact algorithm was derived by Cheng and Zhang [23]. However, an efficient and robust contact algorithm is essential in the 3-D NMM for problems with high-density of discontinuum (e.g., jointed rock mass analysis).

The contact constraint can be considered as an important branch of uncertain boundary conditions. The uncertainties originate from two main sources: (1) contact position, contact zone size and contact status are unknown prior to solution, and also all changing through the time; (2) three criteria must be satisfied during whole contact process: no penetration among contact bodies, no tensile force at the contact interface and frictional constitutive condition in tangential direction. A contact brings the third type of nonlinearity into solid mechanics, namely, contact interface nonlinearity, besides the material nonlinearity and the geometric nonlinearity.

Contact involves two main issues: contact detection and contact enforcement. Although contact problem has been raised for hundreds of years, contact detection has only attracted attentions since 1990s when the researchers were trying to apply numerical simulations to complicate and dynamic engineering applications such as car crash, fragmentation of brittle material and rock fall hazard.

Contact detection is usually performed in two independent stages. The first stage, referred to as global searching (or neighbor search), is merely a rough search that aims to provide a list of blocks possible in contact. As discussed in [24], it is sufficient at this stage to represent the objects by a coarse description, for example, bounding boxes or surrounding spheres for low computational cost. The advanced algorithms for efficient global searching include Heapsort Algorithm [24], Alternating Digital Tree method [25], Double-Ended Spatial Sorting algorithm [26] and No Binary Search algorithm [27]. In the second stage, called local searching, pairs of contacting blocks obtained from the first stage are examined in more detail to find the real contact pairs. Typical examples for local searching algorithms include Hierarchy Territory Algorithm [28], Splitting Pinball Method [29], Inside-Outside search Algorithm (IOA) [30], Common Plane Method [31], Penetrated Edges Method (PEM) [32], Incision Body scheme [17] and Inscribed Sphere Method [33].

None of the methods could be directly applied to the 3-D NMM because of its unique characteristics. Yet, it is too hasty to say these methods are not good because each algorithm has its own usage and range of application. This paper inherits the techniques from the existing contact detection algorithms, either developed for continuum methods or discontinuum methods, and makes necessary modifications to fit the 3-D NMM framework considering its unique features.

After contact detection procedure, locations of contacting zones are confirmed. The contact interface condition builds up modified energy functional as an additional constraint to unknown \mathbf{u}

$$\Pi^* = \Pi_u + \Pi_c \quad (1)$$

where Π_u is total energy without contact constraint condition and Π_c indicates the component caused by contact constraints. There are several different strategies to find the maximum/minimum of a function subject to constraints, such as the penalty method [1], the Lagrange Multiplier method, the Augmented Lagrange Multiplier method [34], the method of direct elimination of the geometrical contact constraints [35], the barrier method [36] and the cross-constraint method that combines the penalty and barrier methods [37]. Each method has its advantages and drawbacks. Most standard numerical codes (e.g., ANSYS, LS-DYNA, 3-DEC and 2-D DDA/NMM), which are able to handle contact problems, use one of the first three methods. This paper utilizes the first method.

The remainder of the paper is organized as follows. The difficulties and unique characteristics of the contact detection in the 3-D NMM will be discussed in Section 2. A customized contact detection algorithm for the 3-D NMM will be presented in Section 3. The penalty method will then be selected to enforce the contact constraints in Section 4, and a general contact solution procedure in the 3-D NMM (implicit time integration) is laid out in Section 5. Three typical examples are finally simulated to calibrate the proposed contact algorithms in Section 6.

2. DIFFICULTIES AND CHARACTERISTICS OF CONTACT DETECTION TECHNIQUE IN 3-D NMM

2.1. Basic concepts of the NMM

The NMM is a specific application of a topological concept ‘manifold’ into numerical method in engineering. It employs a set of small patches to cover the problem domain, and each small patch is termed as a mathematical cover. These small patches are allowed to overlap each other, span discontinuities and even be partially out of the material volume. The only requirement is that the union of the small patches must be large enough to completely cover the problem domain. The physical features including the external boundary and the internal discontinuities may intersect each mathematical cover into several isolated pieces. Each piece, if it is within the problem domain, forms a physical cover. The common region of several overlapped physical covers is termed as a manifold element. Piecing together all the manifold elements produces a complete description of the whole problem domain.

In a typical implementation, it is convenient to use structured finite element meshes to cover the problem domain. The mesh, which is independent to the physical features of the problem domain, is the so-called mathematical mesh. Each finite element or its regular cluster in the mesh is termed as a mathematical cell, while the nodes on the mesh are redefined as stars. The union of all the elements sharing a common star forms a mathematical cover. The isolated piece of the mathematical cover by the discontinuities or boundaries, if it is within the problem domain, is a physical cover. The overlapped region of the physical covers is a manifold element.

The definition of the unique components in the NMM could be found in [1]. The generation of mathematical covers and construction of global approximations in 3-D domain can refer to [20].

2.2. Characteristics of contact detection technique in 3-D NMM

Particular features of the contact detection in the 3-D NMM lie in three aspects:

- The NMM is designed for jointed rock mass analysis. The rock blocks isolated by the joint network may take arbitrary shapes (convex or non-convex).
- Although regular mesh is utilized, the elements may take arbitrary shapes bounded by arbitrarily shaped polygonal facet (convex or non-convex) as a result of the intersection by the discontinuities.
- The NMM is born with the regular mathematical mesh, which could be used as a rough description of the rock block/manifold element in global searching, instead of introducing additional bounding boxes or surrounding spheres.

Because of the listed particular features, many existing contact detection algorithms, developed for either continuum or discontinuum methods, cannot be directly applied to the 3-D NMM. Take the IOA [30] for example, IOA is a highly efficient local detection algorithm, developed under the FEM. IOA works well in the FEM, as its contact facets are always convex (either triangles or convex quadrilateral), and thus, it is straightforward to determine whether one projection point is inside a contact facet or not, by making use of fencing edge equations. However, the second particular feature disables the usage of the IOA in the 3-D NMM.

Another example is the PEM [32]. The PEM assumes that two contact bodies must be convex, or at least locally convex, to guarantee their intersection to be convex too. The first particular feature obviously violates the prerequisite of the PEM. Even though a concave body can be decomposed into a set of convex bodies, there is no stable encoding available to realize the massive decomposition process up until now. If utilizing the current subdivision algorithm directly, it will bring disproportional overburden to the 3-D NMM solution.

This paper customizes a contact detection algorithm specific to the 3-D NMM through considering both its unique characteristics and at the same time inheriting those existing contact detection algorithms when necessary.

3. CONTACT DETECTION IN 3-D NMM

The contact detection in the 3-D NMM is realized via six steps: (1) setup (to setup the hierarchical contact system), (2) warning (to detect pairs of contact blocks and contact manifold elements), (3) matching (to setup contact territory and match primitive level hierarchical contact pairs), (4) transforming (to transform all the contact pair candidates into any one of the two entrance modes), (5) judging (to calculate penetration depth and screen real contact pair) and (6) recording (to record contact pair information for next iteration step or time step). Details are provided in the following six sections, respectively.

3.1. Step 1: setup

The first step is to setup hierarchical contact system and outer normal vector of hierarchies. The so-called hierarchical contact system is an efficient contact detection scheme established for the 3-D NMM. The system consists of five levels of hierarchies, which are contact body, contact manifold element, contact facet, contact edge and contact vertex. Figure 1 assumes a solid polyhedron as a *contact body* placed in mathematical mesh, and the polyhedron is discretized into many manifold elements according to the NMM definition. There are two kinds of elements. One is internal elements, and the other is external elements, attached by contact boundary surface. The latter is referred to as *contact manifold element*. Contact manifold element, itself, is a collection of facet. The external facets, which are on the contact boundary, are defined as *contact facet*. Each contact facet is again defined by *contact edge*. Contact edge normally embodies two *contact vertices*. The tree structure of hierarchical contact system and its referred concepts are illustrated in Figure 2.

The side of the contact facet where the contact happens is defined as the positive side. The local indices of the vertexes of the contact facet are numbered in such a way that its normal vector points to the positive side, as shown in Figure 3. Vertices of a contact facet may not stay on the same plane. The normal vector on the positive side of the contact facet is then defined as

$$\tilde{\mathbf{N}} = \text{nor} \left[\frac{\sum_{i=1}^{n-1} \mathbf{e}_i \times \mathbf{e}_{i+1}}{n} \right] \quad (2)$$

where n is the total edge number of the facet, \mathbf{e}_i unit vector of edge i and ‘nor’ normalizes the vector into a unit vector.

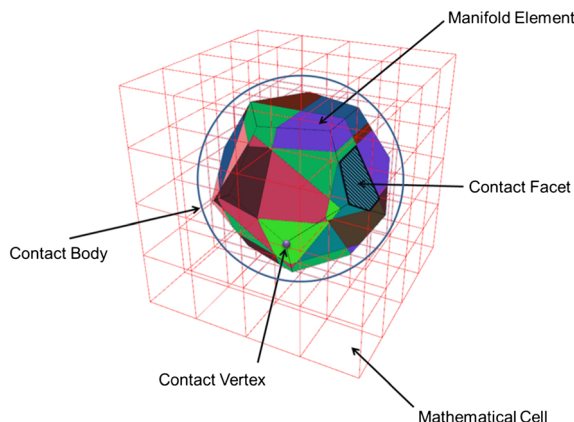


Figure 1. Illustration of hierarchical contact component in three-dimensional numerical manifold method.

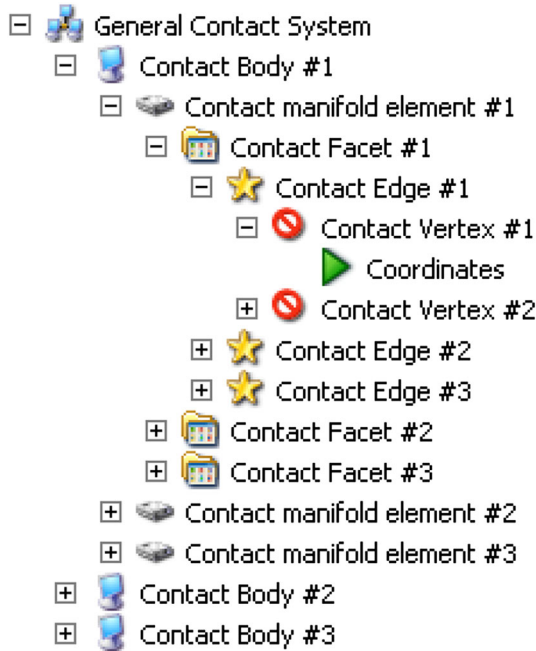


Figure 2. Illustration of hierarchical contact structure in 3-D NMM.

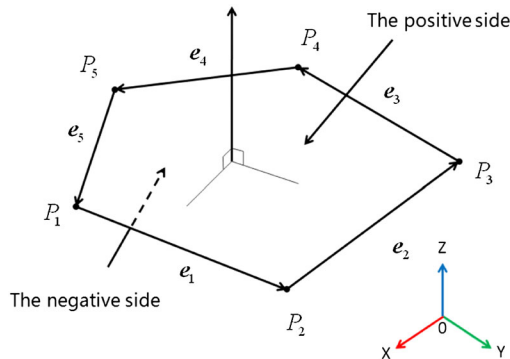


Figure 3. Contact facet with external normal.

3.2. Step 2: warning

This step is to do contact warning using the single block cutting methodology [20].

In the NMM, mathematical cells enclosure the contact manifold element and also the contact body. As illustrated in Figure 4, when two contact bodies continue to approach each other, the mathematical cells would overlap prior to real contact. Based on this fact, we can provide contact warning in advance.

The frame of mathematical cells that enclose the contact body is defined as its contact territory. Its 2-D representation is provided in Figure 5. Pairs of contact bodies are identified when overlapped contact territories are detected.

Considering the geographic features of the mathematical cells in the current 3-D NMM, the single block cutting methodology [20] is utilized to detect the overlapping of two mathematical cells. In analytic geometry introduced in the block theory [38], an infinite plane is normally described by the point-normal equation. An infinite plane divides the 3-D space into upper half-space and lower half-space, each of which is described by an inequality equation. A mathematical cell as one cube can be described by a set of six inequality equations. Similarly, the intersection of two mathematical cells

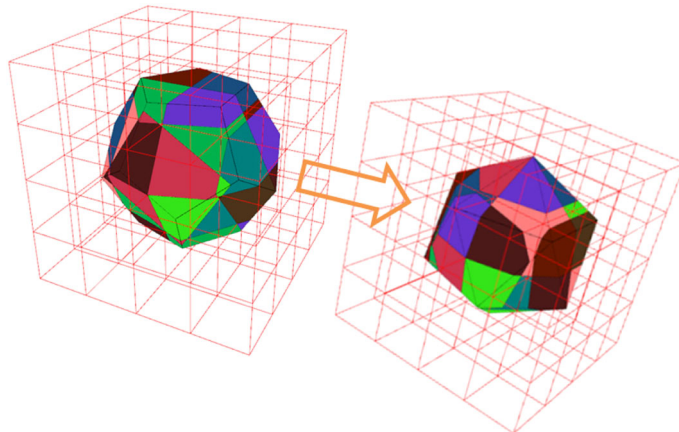


Figure 4. Mathematical cells overlap before real contact of two bodies.

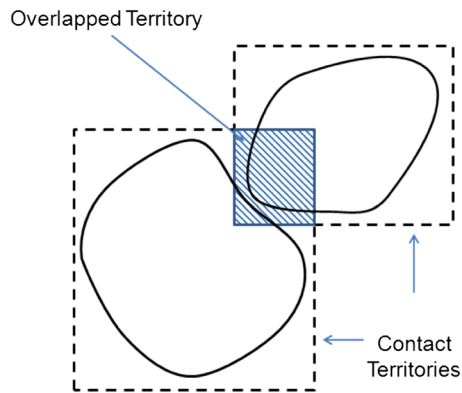


Figure 5. Overlapped territory of two contact bodies.

could be described by the set of 12 inequality equations. If the solution to the set of 12 inequality equations is empty, the two mathematical cells do not overlap, otherwise, they must intersect with each other.

In the proposed method, the intersection body typically is a polyhedron. The subset of the intersected polyhedron includes oriented facets, edges and vertexes. The topological information of the intersected polyhedron can be represented by the following: (1) the geometric information including location, geometric size and the direction to the subsets of the polyhedron; and 2) the topological relationship to these subsets.

The geometrical and topological information is essentially indispensable to completely describe a polyhedron. Complete block information can be represented by a series of facets, which form the polyhedron and material index number. Each facet has a plane equation with a half-space index and a material index. The loop component of each facet consists of a series of vertices with a certain sequence. Supplementary information such as the total number of vertex and the total number of faces is also provided.

Once confirmed, the simplex integration formulation [39] is used to evaluate the volume of the intersected territory. A negative volume means that the two bodies are not coming into contact; thus, further testing on lower level hierarchical components can be trivially rejected. Otherwise, contact warning is activated. Using this strategy, potential contact manifold element pairs could also be detected. Further testing continues for primitive hierarchies (including contact facet, edge and vertex), which is the main task of the next step.

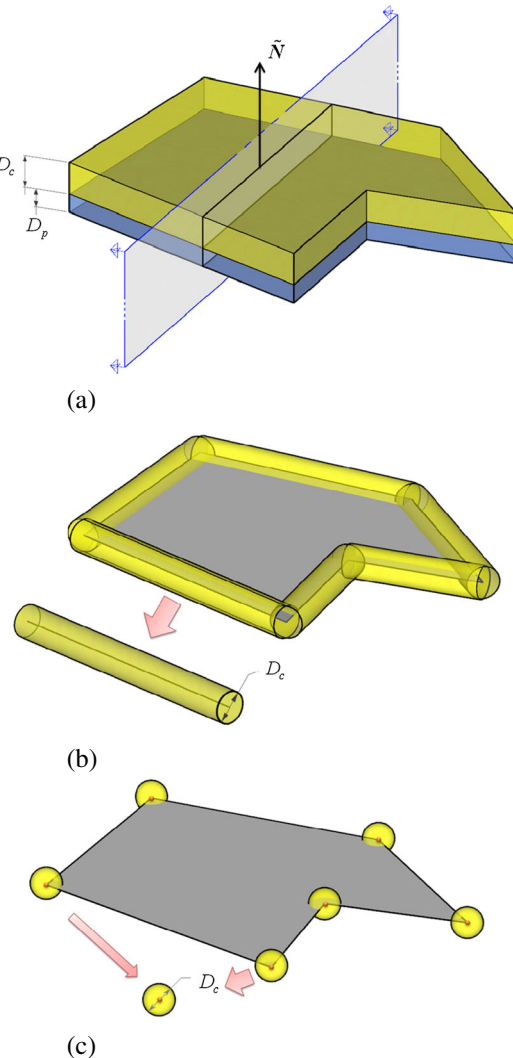


Figure 6. Definition of territory for: (a) contact facet; (b) contact edge; and (c) contact vertex.

3.3. Step 3: matching

Matching process is to define contact territory for primitive hierarchies and match primitive hierarchical contact pair.

Definition of the contact territory for primitive hierarchies follows the criterion that all candidate objects approaching the target object would be caught and tested for contact matching before the interpenetration occurs, as illustrated in Figure 6, where D_c is the territory expansion and controlled by the prescribed maximum vertex displacement within a single time step (equivalent to maximum displacement ratio in 2-D NMM [1]).

Assisting by the contact territory, five basic types of primitive hierarchy contact pairs (e.g., vertex-to-facet, edge-to-edge (crossing), edge-to-edge (parallel), vertex-to-edge and vertex-to-vertex) are detected as shown in Figure 7. Other contacts such as edge-to-facet and facet-to-facet are actually the combination of these five basic types.

After matching check guaranteed by the contact territory intersection detection, a second matching check is designed to avoid possible missed contact pairs, based on the concept of target neighbor. A target neighbor is a collection of one of primitive contact hierarchies and its neighboring contact facet (including its belongings). The target neighbor can be categorized into three groups: vertex-centered target neighbor, edge-centered target neighbor and facet-centered target neighbor, as shown

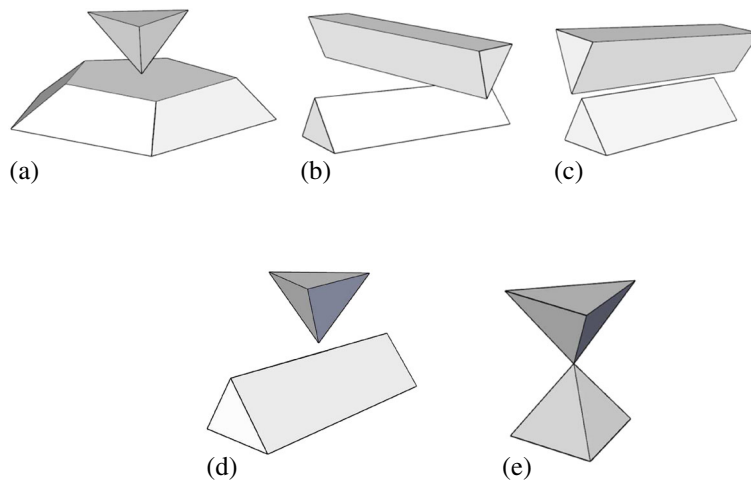


Figure 7. Five basic contact types: (a) vertex-to-facet; (b) edge-to-edge (crossing); (c) edge-to-edge (parallel); (d) vertex-to-edge; and (e) vertex-to-vertex.

in Figure 8. Even though the second matching check might increase the scope of contact detection locally, it ensures the hitting ratio.

During the matching process, useful supplementary information is also provided as follows:

- To build connective network of contact hierarchies, a natural way is to follow the sequential order of the tree structure, that is, each contact hierarchy is defined by specifying all its contact hierarchies at one level lower in a prescribed order. However, it is not an efficient connectivity definition. For example, it requires ergodic operation on whole data structure to determine target neighbors of one vertex. Actually, an alternative way is to reorganize the data structure at an initial stage before calculation. Starting from the lowest-level hierarchy, the information of the vertex starts to expand to include its parent hierarchies' indexes and neighbored primitive hierarchies' indexes, not only the original coordinates. Similar extensions are operated for edge and facet. Obviously, it requires more storage space but saves computation time by avoiding repeatedly extracting the contact vertex information for the contact boundary. It can be considered as an example of the trade-off between the computational efficiency and the storage cost in the contact checking process.
- During the expansion of contact territory, it is possible that some particular contact pair belongs to multiple types. For example, a vertex might match to a facet partner, and at the same time, it also matches to an edge partner. For these cases, it follows the rule of ‘complex to simple’, which is vertex-to-vertex > vertex-to-edge > vertex-to-facet > edge-to-edge (crossing). The purpose is to avoid misjudge to complex situation.
- During double matching checks, edge-to-edge contact is searched independently. After finishing the matching operation between vertex and primitive hierarchies, further checking is run between every edge pairs on the contact boundary. This operation can avoid edge penetration problem, which normally happens when a relatively coarse mathematical mesh is used.

3.4. Step 4: transform

This step is to transform all the detected contact pair candidates into entrance mode.

Among the five basic contact types, vertex-to-facet and edge-to-edge (crossing) are defined as entrance modes, renamed as point-to-plane and crossing-lines entrance modes, respectively. Other three basic types of contact pairs are then transformed to one of the two entrances modes, discussed in the next three sections.

3.4.1. Edge-to-edge (parallel). Setup an auxiliary cross-section normal to the edge, so that the 3-D edge-to-edge (parallel) contact can be treated as a 2-D angle-to-angle contact (Figure 9), which has

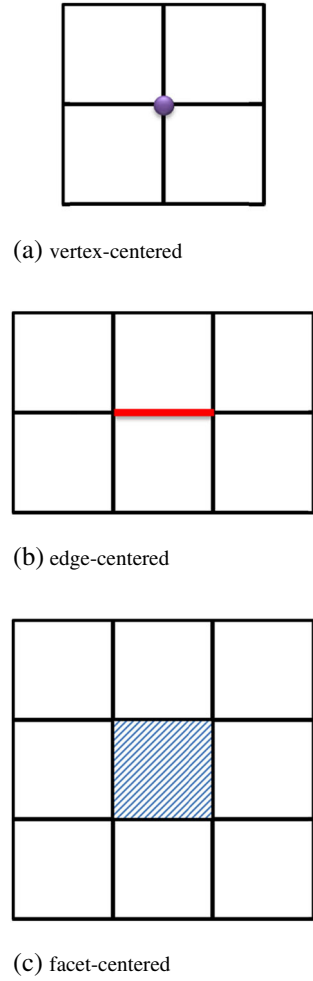


Figure 8. Target neighbors of primitive hierarchies.

been fully discussed in [13]. The only difference is that the entrance lines in 2-D contact should correspond to the entrance planes of 3-D contact cases. By this logic, edge-to-edge (parallel) contact is transformed into one or more pairs of point-to-plane entrance modes.

3.4.2. Vertex-to-edge contact. Each edge is generated by two intersecting facets. The vertex-to-edge specifies the case when vertex is located right above the angle bisector of the edge, and it cannot directly transform to any of the entrance modes in geometric sense. In this case, we have to track the motion velocity of the vertex in last time step. Corresponding entrance mode is targeted by extending vector of vertex velocity. It means that the transforming here is path-dependent, which is different with pure contact judgment based on geometric conditions in previous description. If still unavailable, one possible way is to define a normal vector on the edge by taking the average of normal vectors of all facets sharing the same point of interests, as shown in Figure 10. An auxiliary plane is then constructed perpendicular to the average normal direction, and vertex-to-edge contact is finally transformed to the point-to-plane entrance mode.

3.4.3. Vertex-to-vertex contact. Sharp corner contact can be transformed into point-to-plane entrance mode in a similar way by definition of an auxiliary plane, as illustrated in Figure 11.

In real situations, the vertex presented in 3-D corner could be very complicated, such as those in Figure 12. These two cases are referred to as ‘a vertex in the valley’ [30]. We have to setup local

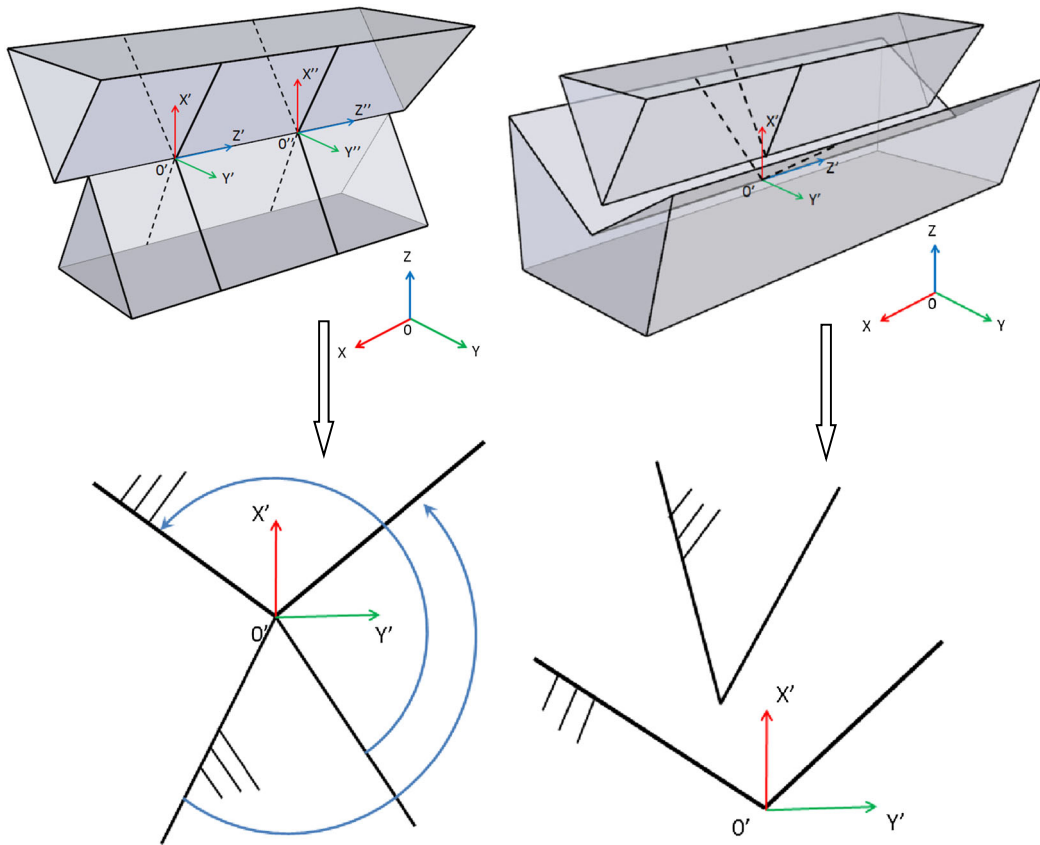


Figure 9. Transform edge-to-edge (parallel) contact to point-to-plane entrance mode.

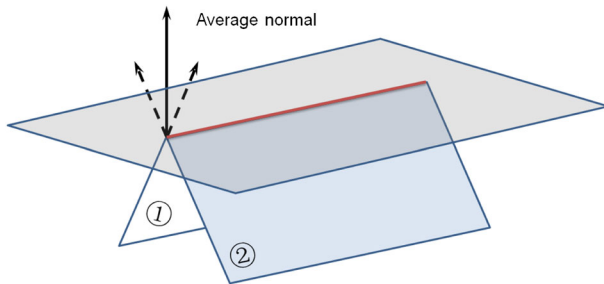


Figure 10. Definition of auxiliary plane for vertex-to-edge contact.

section plane and sample 3-D vertex-to-vertex cases with 2-D slices, to help judgment. It is worth to notice that a vertex in such a valley may have more than one contact pair involving.

3.5. Step 5: judging

Judging process is to locate real contact pair and at the same time guide the selection of the right position to add contact constraints in order to prevent the contact bodies from penetrating each other.

An auxiliary tetrahedron for both modes 1 and 2 is constructed such that a unified formula can be derived to describe the relative position of a contact pair. A point-to-plane entrance mode (mode 1) as shown in Figure 13 is considered. Suppose P_0 is the contact vertex of manifold element α and $P_1 P_2 \dots P_n$ is the contact facet of manifold element β . The vertices of the contact facet may not lie in the same plane; thus, we have to find the most representative two neighboring edges (three neighboring vertices) to form the bottom of an auxiliary tetrahedron. If the cross product by the

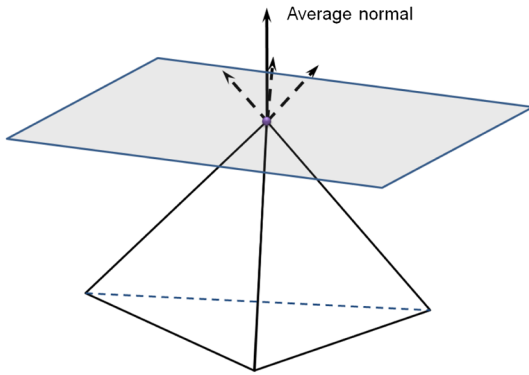


Figure 11. Definition of auxiliary plane for sharp corner contact.

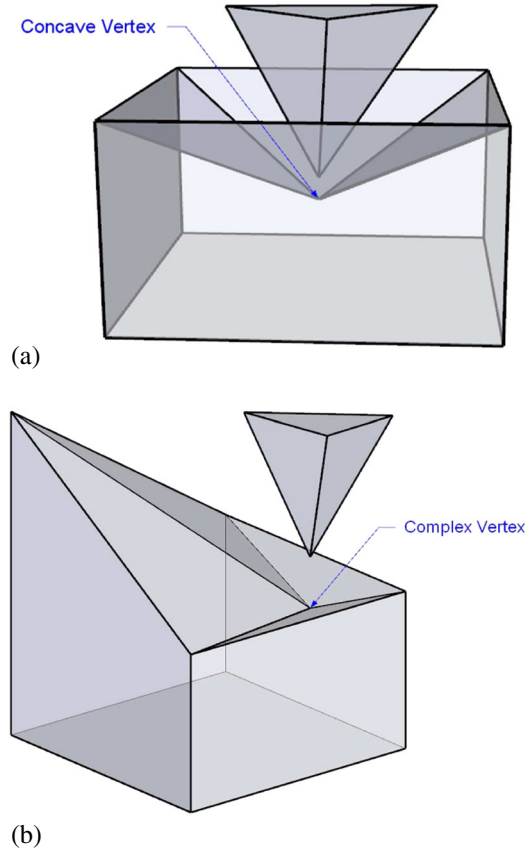


Figure 12. Two examples of complex vertex-to-vertex contacts.

unit vector of two neighbored edges (say, $\overline{P_1 P_2}$ and $\overline{P_2 P_3}$) is closest to the average normal of this contact facet, the three corners of the two edges (P_1, P_2, P_3) are chosen to represent the facet. The chosen criterion is simplified as

$$P_1 \hat{P}_2 P_3 \exists \max \left\{ (\mathbf{e}_i \times \mathbf{e}_{i+1}) \cdot \tilde{\mathbf{N}}, \forall i \in 1 \sim n \right\} \quad (3)$$

where \mathbf{e}_i is unit vector of edge i , ' \exists ' denotes 'choose from', n is the total edge number of the facet and $\tilde{\mathbf{N}}$ is the average normal of the facet, defined in Equation (1).

An auxiliary tetrahedron is constructed as $P_0 P_1 P_2 P_3$. Let $(x_i y_i z_i)$ and $(u_i v_i w_i)$ be the coordinates and displacement increments of vertex P_i , $i = 0 \sim n$, respectively. After the displacement

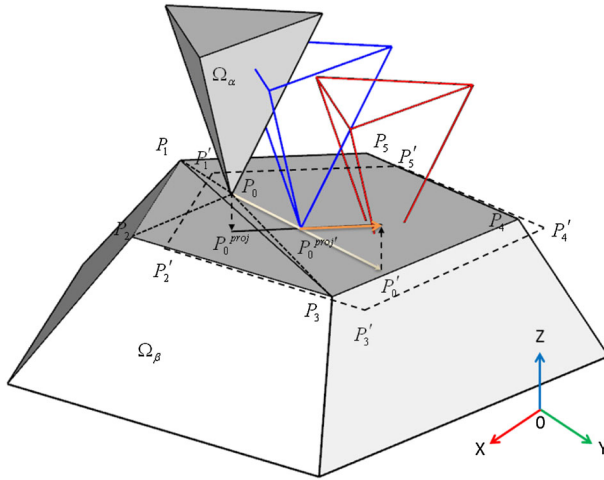


Figure 13. Point-to-plane entrance mode.

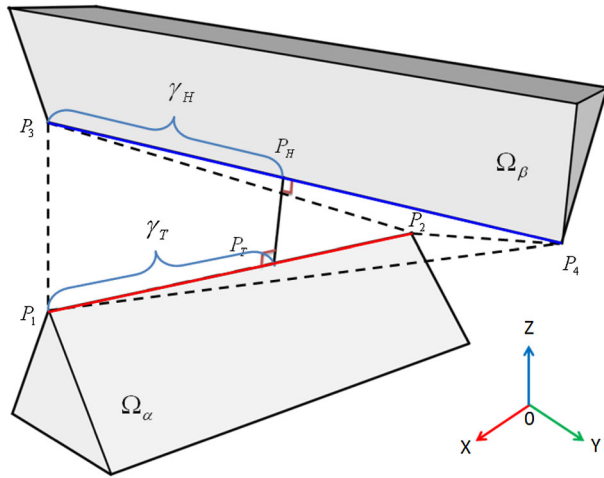


Figure 14. Crossing-lines entrance mode.

increments are applied, the new position of vertexes are depicted as P'_i , $i = 0 \sim n$. The normal distance between the vertex and the facet is

$$d'_N = \frac{1}{A_0} \begin{vmatrix} 1 & x_0 + u_0 & y_0 + v_0 & z_0 + w_0 \\ 1 & x_i + u_i & y_i + v_i & z_i + w_i \\ 1 & x_{i+1} + u_{i+1} & y_{i+1} + v_{i+1} & z_{i+1} + w_{i+1} \\ 1 & x_{i+2} + u_{i+2} & y_{i+2} + v_{i+2} & z_{i+2} + w_{i+2} \end{vmatrix} \quad (4)$$

Neglecting the second and third order infinitesimal terms on the denominator, we have

$$A_0 \approx \sqrt{\left| \begin{array}{cc} y_{i+1} - y_i & z_{i+1} - z_i \\ y_{i+2} - y_i & z_{i+2} - z_i \end{array} \right|^2 + \left| \begin{array}{cc} x_{i+1} - x_i & z_{i+1} - z_i \\ x_{i+2} - x_i & z_{i+2} - z_i \end{array} \right|^2 + \left| \begin{array}{cc} x_{i+1} - x_i & y_{i+1} - y_i \\ x_{i+2} - x_i & y_{i+2} - y_i \end{array} \right|^2} \quad (5)$$

Then, crossing-lines entrance mode (mode 2) is considered, and it is shown in Figure 14. Suppose P_1P_2 is the contact edge of manifold element α , P_3P_4 is the contact edge of manifold element β . Building up spatial auxiliary tetrahedron with the four vertices $(P_3P_1P_2P_4)$ is illustrated in Figure 15(a). Figure 15(a–c) demonstrates the changing situation of auxiliary tetrahedron during the approaching and penetration process. Clearly, the volume of auxiliary tetrahedron also experiences the process from positive to negative.

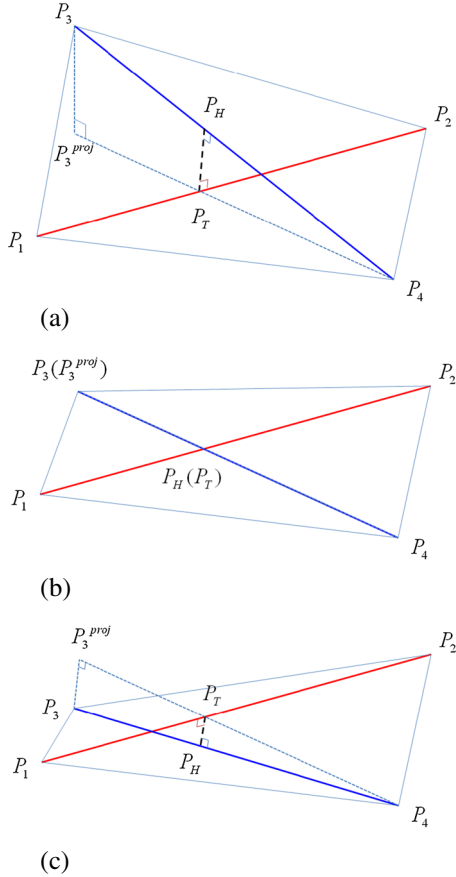


Figure 15. Auxiliary tetrahedron changes during two edges approaching and finally penetrated.

Assume the contact points at line $\overline{P_1P_2}$ and $\overline{P_3P_4}$ as P_H and P_T , respectively. Let (x_i, y_i, z_i) and (u_i, v_i, w_i) be the coordinates and displacement increments of vertex $P_i, i = 1 \sim 4, H, T$. Define

$$\gamma_T = \frac{\left| \overrightarrow{P_1P_T} \right|}{\left| \overrightarrow{P_1P_2} \right|} \quad (6)$$

$$\gamma_H = \frac{\left| \overrightarrow{P_3P_H} \right|}{\left| \overrightarrow{P_3P_4} \right|} \quad (7)$$

Because $\overrightarrow{P_3^{proj}P_3}$ and $\overrightarrow{P_HP_T}$ are relatively small, it can represent each other in geometric sense, where their included angle is ignorable. Therefore,

$$\frac{\overrightarrow{P_HP_T}}{\overrightarrow{P_3^{proj}P_3}} \approx 1 - \gamma_H \quad (8)$$

The normal distance between the two crossing edges is obtained as

$$d'_N = \frac{1 - \gamma_H}{A_0} \begin{vmatrix} 1 & x_3 + u_3 & y_3 + v_3 & z_3 + w_3 \\ 1 & x_1 + u_1 & y_1 + v_1 & z_1 + w_1 \\ 1 & x_4 + u_4 & y_4 + v_4 & z_4 + w_4 \\ 1 & x_2 + u_2 & y_2 + v_2 & z_2 + w_2 \end{vmatrix} \quad (9)$$

Neglecting the second and third order infinitesimal terms on denominator, we have

$$A_0 \approx \sqrt{\left| \begin{array}{cc} y_4 - y_1 & z_4 - z_1 \\ y_2 - y_1 & z_2 - z_1 \end{array} \right|^2 + \left| \begin{array}{cc} x_4 - x_1 & z_4 - z_1 \\ x_2 - x_1 & z_2 - z_1 \end{array} \right|^2 + \left| \begin{array}{cc} x_4 - x_1 & y_4 - y_1 \\ x_2 - x_1 & y_2 - y_1 \end{array} \right|^2} \quad (10)$$

For point-to-plane entrance mode, we renumber the four vertices of the auxiliary tetrahedron as 0→1, 1→2, 2→3, 3→4. For the crossing-lines entrance mode, we renumber the four vertices as 1→2, 2→4, 3→1, 4→3. Then, the normal distance for the two entrance modes can be written as a unified form

$$d'_N = \frac{1-\gamma}{A_0} \left| \begin{array}{cccc} 1 & x_1 + u_1 & y_1 + v_1 & z_1 + w_1 \\ 1 & x_2 + u_2 & y_2 + v_2 & z_2 + w_2 \\ 1 & x_3 + u_3 & y_3 + v_3 & z_3 + w_3 \\ 1 & x_4 + u_4 & y_4 + v_4 & z_4 + w_4 \end{array} \right|, \quad \begin{array}{l} \gamma = 0 \text{ for mode 1} \\ \gamma = \gamma_H \text{ for mode 2} \end{array} \quad (11)$$

If $d'_N < 0$, penetration takes place and the contact pair candidate is labeled as a real contact pair.

3.6. Step 6: recording

Recording process is to record real contact pair information for next iteration step or time step. The recording information includes contact pair index, contact pair types, the number of entrance modes for current contact pair, open-close status, penetration depth, relative tangential displacement and new contact identity. The purpose to record the information is to reduce the computational costs.

Remarks

In the proposed algorithm for the 3-D NMM, the mathematical mesh has been utilized for three purposes. Firstly, it is used to generate the manifold elements and to interpolate the approximation field, as introduction in Section 2.1.

Secondly, it is to form the contact territories for the contact body and contact manifold element. In the processing of these two purposes, the mathematical mesh moves together with the motion of the body enclosed, described by Lagrangian scheme.

At the same time, the initial mathematical mesh stays still at its original position and does not move with the calculation. It serves for the third purpose as to generate the position code of the contact object. In the current 3-D NMM, a spatial sorting algorithm is implemented to further enhance the contact computational efficiency. The space is divided into grid cells, and each cell is allocated a one-dimensional (1-D) index. If an object occupies the cell, the corresponding 1-D index is assigned to the object. Only objects sharing the same index are checked for possible contact. The initial mathematical mesh is used as the grid cell for spatial sorting. The mesh is fixed, but the objects move together with the changing 1-D index. The spatial sorting procedure is triggered when necessary. For example, it is used for the contact warning when many blocks are in a coarse mesh, while can also be triggered at the matching process when few blocks are in a fine mesh.

4. PENALTY TREATMENT OF CONTACT CONSTRAINTS IN 3-D NMM

Each contact pair has totally three statuses: stick, slide and separate, as shown in Table I. The operations when contact status has been changed are listed in Table II. The 3-D NMM employs the penalty method to impose the contact constraints into system functional and realizes the contact constraints through adding or removing penalty springs and/or frictional forces. Penalty terms due to the contact constraints are added to system functional as

$$\Pi_c^{\text{Penalty}} = \frac{1}{2} \int_{\Gamma_c} \left(k_N \cdot (d'_N)^2 + k_T \cdot (d'_T)^2 \right) dA, \quad k_N, k_T > 0 \quad (12)$$

Table I. Possible contact modes for each contact pair.

Contact status	Verification
Separate	$(t+\Delta t \mathbf{x}^B - t+\Delta t \mathbf{x}^A) \cdot t+\Delta t \mathbf{n}_3^B \geq \varepsilon_s$, If not, turn to 'stick state'; record the position of contact
Contact	a) $t+\Delta t \mathbf{P}_N^A = -t+\Delta t \mathbf{P}_N^B \geq 0$, if not, turn to 'separate state' b) $ t+\Delta t \mathbf{P}_T^i - \mu \cdot t+\Delta t \mathbf{P}_N^i < 0 \quad (i = A, B)$, if not, turn to 'slide state'
	a) $t+\Delta t \mathbf{P}_N^A = -t+\Delta t \mathbf{P}_N^B \geq 0$, if not, turn to 'separate state' b) $(t+\Delta t \mathbf{u}_T^A - t+\Delta t \mathbf{u}_T^B)^T + \Delta t \mathbf{P}_T^A < 0$, $ t+\Delta t \mathbf{u}_T^A - t+\Delta t \mathbf{u}_T^B < \varepsilon_s$, if not, turn to 'stick state'

ε_s , the allowable tolerance in contact checking procedure; \mathbf{x} , the coordinates; \mathbf{u} , the displacement; \mathbf{P}_N , the normal contact force; \mathbf{P}_T , the tangential contact traction or friction force in tangential contact condition; μ , frictional coefficient.

Table II. Detailed operation corresponding to the change of contact state.

State changes	Corresponding operation
Separate to separate	No change
Separate to slide	Apply the normal spring and a pair of friction force
Separate to stick	Apply the normal and tangential springs
Slide to separate	Release the normal spring and a pair of friction force
Slide to slide	No change
Slide to stick	Release the friction forces and apply the tangential spring
Stick to separate	Release the normal and tangential springs
Stick to slide	Release the tangential spring and apply a pair of friction force
Stick to stick	No change

where k_N and k_T are the stiffness of normal spring and tangential spring, respectively, d'_N and d'_T are the penetration depth in the normal direction and the relative displacement along the tangential direction, respectively.

4.1. Sub-matrices due to normal spring

From Equation (11),

$$d'_N = \frac{1-\gamma}{A_0} \begin{vmatrix} 1 & x_1 + u_1 & y_1 + v_1 & z_1 + w_1 \\ 1 & x_2 + u_2 & y_2 + v_2 & z_2 + w_2 \\ 1 & x_3 + u_3 & y_3 + v_3 & z_3 + w_3 \\ 1 & x_4 + u_4 & y_4 + v_4 & z_4 + w_4 \end{vmatrix} \\ = \frac{1-\gamma}{A_0} \left(V_0 + \begin{vmatrix} 1 & u_1 & y_1 & z_1 \\ 1 & u_2 & y_2 & z_2 \\ 1 & u_3 & y_3 & z_3 \\ 1 & u_4 & y_4 & z_4 \end{vmatrix} + \begin{vmatrix} 1 & x_1 & v_1 & z_1 \\ 1 & x_2 & v_2 & z_2 \\ 1 & x_3 & v_3 & z_3 \\ 1 & x_4 & v_4 & z_4 \end{vmatrix} + \begin{vmatrix} 1 & x_1 & y_1 & w_1 \\ 1 & x_2 & y_2 & w_2 \\ 1 & x_3 & y_3 & w_3 \\ 1 & x_4 & y_4 & w_4 \end{vmatrix} + \begin{vmatrix} 1 & u_1 & v_1 & w_1 \\ 1 & u_2 & v_2 & w_2 \\ 1 & u_3 & v_3 & w_3 \\ 1 & u_4 & v_4 & w_4 \end{vmatrix} \right) \quad (13)$$

where

$$V_0 = \begin{vmatrix} 1 & x_1 & y_1 & z_1 \\ 1 & x_2 & y_2 & z_2 \\ 1 & x_3 & y_3 & z_3 \\ 1 & x_4 & y_4 & z_4 \end{vmatrix} \quad (14)$$

Let C_{ij} be the algebraic complement of determinant V_0 about element v_{ij} , denoted as

$$C_{ij} = (-1)^{i+j} \cdot V_{ij} \quad (15)$$

where V_{ij} is cofactor of V_0 about element v_{ij} . For example,

$$C_{12} = (-1)^{1+2} \cdot \begin{vmatrix} 1 & y_2 & z_2 \\ 1 & y_3 & z_3 \\ 1 & y_4 & z_4 \end{vmatrix} \quad (16)$$

Neglecting the infinitesimal terms (last term in Equation (13)), the increment of the normal penetration distance is

$$d'_N = \frac{1-\gamma}{A_0} \left\{ \begin{array}{l} (C_{12} \ C_{13} \ C_{14}) \begin{bmatrix} u_1 \\ v_1 \\ w_1 \end{bmatrix} + (C_{22} \ C_{23} \ C_{24}) \begin{bmatrix} u_2 \\ v_2 \\ w_2 \end{bmatrix} \\ + (C_{32} \ C_{33} \ C_{34}) \begin{bmatrix} u_3 \\ v_3 \\ w_3 \end{bmatrix} + (C_{42} \ C_{43} \ C_{44}) \begin{bmatrix} u_4 \\ v_4 \\ w_4 \end{bmatrix} \end{array} \right\} \quad (17)$$

For mode 1, let

$$\begin{aligned} \mathbf{H} &= \frac{1-\gamma}{A_0} [T_\alpha(x_1, y_1, z_1)]^T \begin{bmatrix} C_{12} \\ C_{13} \\ C_{14} \end{bmatrix} \\ \mathbf{G} &= \frac{1-\gamma}{A_0} \left\{ [T_\beta(x_2, y_2, z_2)]^T \begin{bmatrix} C_{22} \\ C_{23} \\ C_{24} \end{bmatrix} + [T_\beta(x_3, y_3, z_3)]^T \begin{bmatrix} C_{32} \\ C_{33} \\ C_{34} \end{bmatrix} + [T_\beta(x_4, y_4, z_4)]^T \begin{bmatrix} C_{42} \\ C_{43} \\ C_{44} \end{bmatrix} \right\} \end{aligned} \quad (18)$$

and similarly for mode 2,

$$\begin{aligned} \mathbf{H} &= \frac{1-\gamma}{A_0} \left\{ [T_\alpha(x_1, y_1, z_1)]^T \begin{bmatrix} C_{22} \\ C_{23} \\ C_{24} \end{bmatrix} + [T_\alpha(x_2, y_2, z_2)]^T \begin{bmatrix} C_{42} \\ C_{43} \\ C_{44} \end{bmatrix} \right\} \\ \mathbf{G} &= \frac{1-\gamma}{A_0} \left\{ [T_\beta(x_3, y_3, z_3)]^T \begin{bmatrix} C_{12} \\ C_{13} \\ C_{14} \end{bmatrix} + [T_\beta(x_4, y_4, z_4)]^T \begin{bmatrix} C_{32} \\ C_{33} \\ C_{34} \end{bmatrix} \right\} \end{aligned} \quad (19)$$

where $[T_\alpha]$ and $[T_\beta]$ are the shape functions of manifold elements α and β , respectively. For mode 1, vertex 1 belongs to manifold element α , and vertices 2 to 4 belong to manifold element β . For mode 2, vertices 2 and 4 belong to manifold element α , and vertices 1 and 3 belong to manifold element β .

Then,

$$d'_N = (1-\gamma) \cdot \left(\mathbf{H}^T \mathbf{D}_\alpha + \mathbf{G}^T \mathbf{D}_\beta + \frac{V_0}{A_0} \right) \quad (20)$$

where \mathbf{D}_α and \mathbf{D}_β are the unknown vectors associated with manifold elements α and β , respectively.

The potential energy due to the normal spring is

$$\begin{aligned} \Pi_N &= (1-\gamma)^2 \frac{k_N}{2} (d'_N)^2 = (1-\gamma)^2 \frac{k_N}{2} \left(\mathbf{H}^T \mathbf{D}_\alpha + \mathbf{G}^T \mathbf{D}_\beta + \frac{V_0}{A_0} \right)^2 \\ &= (1-\gamma)^2 \frac{k_N}{2} \left(\begin{array}{l} \mathbf{D}_\alpha^T \mathbf{H} \mathbf{H}^T \mathbf{D}_\alpha + \mathbf{D}_\beta^T \mathbf{G} \mathbf{G}^T \mathbf{D}_\beta + 2 \mathbf{D}_\alpha^T \mathbf{H} \mathbf{G}^T \mathbf{D}_\beta \\ + 2 \left(\frac{V_0}{A_0} \right) \mathbf{D}_\alpha^T \mathbf{H} + 2 \left(\frac{V_0}{A_0} \right) \mathbf{D}_\beta^T \mathbf{G} + \left(\frac{V_0}{A_0} \right)^2 \end{array} \right) \end{aligned} \quad (21)$$

Thus, in the case of tetrahedral mesh, the sub-matrices due to the normal spring can be obtained and assembled into global stiffness matrix and global loading vector as

$$\begin{aligned}
 (1-\gamma)^2 k_N \mathbf{H}_{\alpha(r)} \mathbf{H}_{\alpha(s)}^T &\rightarrow \mathbf{K}_{\alpha(r)\alpha(s)}, (r,s = 1-4) \\
 (1-\gamma)^2 k_N \mathbf{H}_{\alpha(r)} \mathbf{G}_{\beta(s)}^T &\rightarrow \mathbf{K}_{\alpha(r)\beta(s)}, (r,s = 1-4) \\
 (1-\gamma)^2 k_N \mathbf{G}_{\beta(r)} \mathbf{H}_{\alpha(s)}^T &\rightarrow \mathbf{K}_{\beta(r)\alpha(s)}, (r,s = 1-4) \\
 (1-\gamma)^2 k_N \mathbf{G}_{\beta(r)} \mathbf{G}_{\beta(s)}^T &\rightarrow \mathbf{K}_{\beta(r)\beta(s)}, (r,s = 1-4) \\
 -(1-\gamma)^2 k_N (V_0/A_0) \mathbf{H}_{\alpha(r)} &\rightarrow \mathbf{F}_{\alpha(r)}, (r = 1-4) \\
 -(1-\gamma)^2 k_N (V_0/A_0) \mathbf{G}_{\beta(r)} &\rightarrow \mathbf{F}_{\beta(r)}, (r = 1-4)
 \end{aligned} \tag{22}$$

4.2. Sub-matrices due to tangential spring

Assume $P_1^{\text{proj}}(x_p, y_p, z_p)$ is the projection point of vertex P_1 on reference entrance plane $P_2P_3P_4$. After a time step, P_1 and P_1^{proj} move to P'_1 and $P_1^{\text{proj}'}$, as shown in Figure 15.

There is a tangential penalty spring between P'_1 and $P_1^{\text{proj}'}$ to prevent the tangential displacement on the surface. The vector theory has been used to determine the tangential displacement

$$(d'_T)^2 = \left| \overrightarrow{P'_1 P_1^{\text{proj}'}} \right|^2 - (d'_N)^2 \tag{23}$$

Considering both modes 1 and 2, we have

$$(d'_T)^2 = (1-\gamma)^2 \cdot \left[\left| \overrightarrow{P'_1 P_1^{\text{proj}'}} \right|^2 - \left(\overrightarrow{P'_1 P_1^{\text{proj}'}} \cdot \tilde{\mathbf{N}} \right)^2 \right] \tag{24}$$

where $\tilde{\mathbf{N}}$ denotes the average normal of reference entrance facet, determined from Equation (1). Then,

$$\begin{aligned}
 \Pi_T &= (1-\gamma)^2 \frac{k_T}{2} (d'_T)^2 \\
 &= (1-\gamma)^2 \frac{k_T}{2} \left\{ \begin{bmatrix} x_1 + u_1 - x_p - u_p \\ y_1 + v_1 - y_p - v_p \\ z_1 + w_1 - z_p - w_p \end{bmatrix}^T \begin{bmatrix} x_1 + u_1 - x_p - u_p \\ y_1 + v_1 - y_p - v_p \\ z_1 + w_1 - z_p - w_p \end{bmatrix} \right. \\
 &\quad \left. - \begin{bmatrix} x_1 + u_1 - x_p - u_p \\ y_1 + v_1 - y_p - v_p \\ z_1 + w_1 - z_p - w_p \end{bmatrix}^T \tilde{\mathbf{N}} \cdot \tilde{\mathbf{N}}^T \begin{bmatrix} x_1 + u_1 - x_p - u_p \\ y_1 + v_1 - y_p - v_p \\ z_1 + w_1 - z_p - w_p \end{bmatrix} \right\} \\
 &= (1-\gamma)^2 \frac{k_T}{2} \left\{ \begin{bmatrix} x_1 + u_1 - x_p - u_p \\ y_1 + v_1 - y_p - v_p \\ z_1 + w_1 - z_p - w_p \end{bmatrix}^T [\mathbf{E} - \tilde{\mathbf{N}} \cdot \tilde{\mathbf{N}}^T] \begin{bmatrix} x_1 + u_1 - x_p - u_p \\ y_1 + v_1 - y_p - v_p \\ z_1 + w_1 - z_p - w_p \end{bmatrix} \right\} \\
 &= (1-\gamma)^2 \frac{k_T}{2} \left\{ \begin{bmatrix} x_1 - x_p \\ y_1 - y_p \\ z_1 - z_p \end{bmatrix}^T [\mathbf{E} - \tilde{\mathbf{N}} \cdot \tilde{\mathbf{N}}^T] \begin{bmatrix} x_1 - x_p \\ y_1 - y_p \\ z_1 - z_p \end{bmatrix} + 2 \begin{bmatrix} u_1 - u_p \\ v_1 - v_p \\ w_1 - w_p \end{bmatrix}^T [\mathbf{E} - \tilde{\mathbf{N}} \cdot \tilde{\mathbf{N}}^T] \begin{bmatrix} x_1 - x_p \\ y_1 - y_p \\ z_1 - z_p \end{bmatrix} \right. \\
 &\quad \left. + \begin{bmatrix} u_1 - u_p \\ v_1 - v_p \\ w_1 - w_p \end{bmatrix}^T [\mathbf{E} - \tilde{\mathbf{N}} \cdot \tilde{\mathbf{N}}^T] \begin{bmatrix} u_1 - u_p \\ v_1 - v_p \\ w_1 - w_p \end{bmatrix} \right\}
 \end{aligned} \tag{25}$$

where \mathbf{E} is identity matrix. Therefore,

$$\begin{aligned} \Pi_T &= (1-\gamma)^2 \frac{k_T}{2} (d'_T)^2 \\ &= (1-\gamma)^2 \frac{k_T}{2} \left\{ \begin{array}{l} \left[\begin{array}{c} x_1 - x_p \\ y_1 - y_p \\ z_1 - z_p \end{array} \right]^T \left[\mathbf{E} - \tilde{\mathbf{N}} \cdot \tilde{\mathbf{N}}^T \right] \left[\begin{array}{c} x_1 - x_p \\ y_1 - y_p \\ z_1 - z_p \end{array} \right] \\ + 2 \cdot \mathbf{D}_\alpha^T [T_\alpha(x_1, y_1, z_1)]^T \left[\mathbf{E} - \tilde{\mathbf{N}} \cdot \tilde{\mathbf{N}}^T \right] \left[\begin{array}{c} x_1 - x_p \\ y_1 - y_p \\ z_1 - z_p \end{array} \right] \\ - 2 \cdot \mathbf{D}_\beta^T [T_\beta(x_p, y_p, z_p)]^T \left[\mathbf{E} - \tilde{\mathbf{N}} \cdot \tilde{\mathbf{N}}^T \right] \left[\begin{array}{c} x_1 - x_p \\ y_1 - y_p \\ z_1 - z_p \end{array} \right] \\ + \mathbf{D}_\alpha^T [T_\alpha(x_1, y_1, z_1)]^T \left[\mathbf{E} - \tilde{\mathbf{N}} \cdot \tilde{\mathbf{N}}^T \right] [T_\alpha(x_1, y_1, z_1)] \mathbf{D}_\alpha \\ - \mathbf{D}_\alpha^T [T_\alpha(x_1, y_1, z_1)]^T \left[\mathbf{E} - \tilde{\mathbf{N}} \cdot \tilde{\mathbf{N}}^T \right] [T_\beta(x_p, y_p, z_p)] \mathbf{D}_\beta \\ - \mathbf{D}_\beta^T [T_\beta(x_p, y_p, z_p)]^T \left[\mathbf{E} - \tilde{\mathbf{N}} \cdot \tilde{\mathbf{N}}^T \right] [T_\alpha(x_1, y_1, z_1)] \mathbf{D}_\alpha \\ + \mathbf{D}_\beta^T [T_\beta(x_p, y_p, z_p)]^T \left[\mathbf{E} - \tilde{\mathbf{N}} \cdot \tilde{\mathbf{N}}^T \right] [T_\beta(x_p, y_p, z_p)] \mathbf{D}_\beta \end{array} \right\} \end{aligned} \quad (26)$$

Let

$$\begin{aligned} \tilde{\mathbf{H}} &= [T_\alpha(x_1, y_1, z_1)]^T \\ \tilde{\mathbf{G}} &= [T_\beta(x_p, y_p, z_p)]^T \end{aligned} \quad (27)$$

Finally, the sub-matrices due to the tangential spring are obtained and assembled to the global stiffness matrix and global loading vector as

$$\begin{aligned} &(1-\gamma)^2 k_T \tilde{\mathbf{H}}_{\alpha(r)} \left[\mathbf{E} - \tilde{\mathbf{N}} \cdot \tilde{\mathbf{N}}^T \right] \tilde{\mathbf{H}}_{\alpha(s)}^T \rightarrow \mathbf{K}_{\alpha(r)\alpha(s)}, (r, s = 1-4) \\ &-(1-\gamma)^2 k_T \tilde{\mathbf{H}}_{\alpha(r)} \left[\mathbf{E} - \tilde{\mathbf{N}} \cdot \tilde{\mathbf{N}}^T \right] \tilde{\mathbf{H}}_{\beta(s)}^T \rightarrow \mathbf{K}_{\alpha(r)\beta(s)}, (r, s = 1-4) \\ &-(1-\gamma)^2 k_T \tilde{\mathbf{H}}_{\beta(r)} \left[\mathbf{E} - \tilde{\mathbf{N}} \cdot \tilde{\mathbf{N}}^T \right] \tilde{\mathbf{H}}_{\alpha(s)}^T \rightarrow \mathbf{K}_{\beta(r)\alpha(s)}, (r, s = 1-4) \\ &(1-\gamma)^2 k_T \tilde{\mathbf{H}}_{\beta(r)} \left[\mathbf{E} - \tilde{\mathbf{N}} \cdot \tilde{\mathbf{N}}^T \right] \tilde{\mathbf{H}}_{\beta(s)}^T \rightarrow \mathbf{K}_{\beta(r)\beta(s)}, (r, s = 1-4) \\ &-(1-\gamma)^2 k_T \tilde{\mathbf{H}}_{\alpha(r)} \left[\mathbf{E} - \tilde{\mathbf{N}} \cdot \tilde{\mathbf{N}}^T \right] \left[\begin{array}{c} x_1 - x_p \\ y_1 - y_p \\ z_1 - z_p \end{array} \right] \rightarrow \mathbf{F}_{\alpha(r)}, (r, s = 1-4) \\ &-(1-\gamma)^2 k_T \tilde{\mathbf{G}}_{\beta(r)} \left[\mathbf{E} - \tilde{\mathbf{N}} \cdot \tilde{\mathbf{N}}^T \right] \left[\begin{array}{c} x_1 - x_p \\ y_1 - y_p \\ z_1 - z_p \end{array} \right] \rightarrow \mathbf{F}_{\beta(r)}, (r, s = 1-4) \end{aligned} \quad (28)$$

4.3. Sub-matrices due to frictional force

For the sliding contact, beside the normal spring, a pair of frictional forces will be added instead of a tangential spring. Based on the Coulomb's friction law, the frictional force is calculated as

$$|\mathbf{f}| = \text{sign} \cdot \mu \cdot k_N d'_N \quad (29)$$

where 'sign' is assigned as '+' or '-' according to the direction of relative sliding, μ is the friction coefficient and $k_N d'_N$ is the normal force.

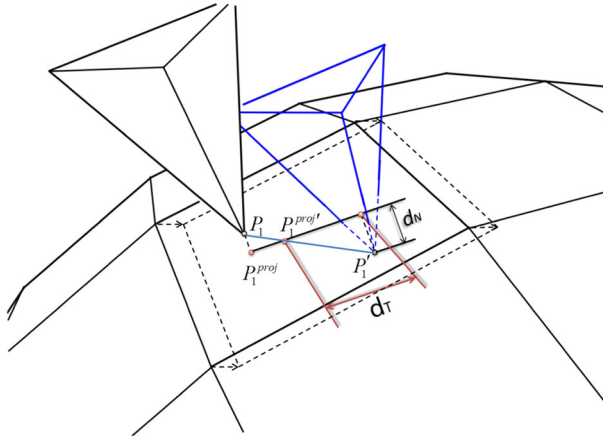


Figure 16. Representation of shear displacement.

As shown in Figure 16, the tangential vector of relative sliding on the contact facets is

$$\mathbf{d}'_F = \overrightarrow{P'_1 P_1^{\text{proj}'}} - \left(\overrightarrow{P'_1 P_1^{\text{proj}'}} \cdot \tilde{\mathbf{N}} \right) \tilde{\mathbf{N}} \quad (30)$$

Then, the potential energy due to frictional force \mathbf{f} is

$$\Pi_F = \mathbf{f} \cdot \mathbf{d}'_F = |\mathbf{f}| \cdot |\mathbf{d}'_F| = |\mathbf{f}| \cdot \begin{bmatrix} u_1 - u_p \\ v_1 - v_p \\ w_1 - w_p \end{bmatrix}^T \begin{bmatrix} \frac{d'_{F_x}}{|\mathbf{d}'_F|} \\ \frac{d'_{F_y}}{|\mathbf{d}'_F|} \\ \frac{d'_{F_z}}{|\mathbf{d}'_F|} \end{bmatrix} = |\mathbf{f}| \cdot \mathbf{D}_\alpha^T \bar{\mathbf{H}} - |\mathbf{f}| \cdot \mathbf{D}_\beta^T \bar{\mathbf{G}} \quad (31)$$

where

$$\bar{\mathbf{H}} = \mathbf{T}_\alpha^T (x_1, y_1, z_1) \begin{bmatrix} \frac{d'_{F_x}}{|\mathbf{d}'_F|} \\ \frac{d'_{F_y}}{|\mathbf{d}'_F|} \\ \frac{d'_{F_z}}{|\mathbf{d}'_F|} \end{bmatrix}, \quad \bar{\mathbf{G}} = \mathbf{T}_\beta^T (x_p, y_p, z_p) \begin{bmatrix} \frac{d'_{F_x}}{|\mathbf{d}'_F|} \\ \frac{d'_{F_y}}{|\mathbf{d}'_F|} \\ \frac{d'_{F_z}}{|\mathbf{d}'_F|} \end{bmatrix} \quad (32)$$

The sub-matrices due to the frictional force are obtained and assembled to the global loading vector as

$$\begin{aligned} & (1 - \gamma) |\mathbf{f}| \bar{\mathbf{H}}_{\alpha(r)} \rightarrow \mathbf{F}_{\alpha(r)}, \quad (r = 1 - 4) \\ & -(1 - \gamma) |\mathbf{f}| \bar{\mathbf{G}}_{\beta(r)} \rightarrow \mathbf{F}_{\beta(r)}, \quad (r = 1 - 4) \end{aligned} \quad (33)$$

5. GENERAL PROCEDURE FOR 3-D NMM ANALYSIS

This section presents a general incremental solution scheme with contact treatment capacity within the 3-D NMM framework. It combines the aforementioned techniques to generalize the solution procedure, including the mechanics condition of contact interface, the contact detection algorithm and the penalty method for incorporating contact constraints into system functional based on generalized variational principle.

5.1. Open-close iteration

As a matter of fact, the requirement of the contact treatment is very strict under the implicit scheme framework. The reason is that the implicit method needs the system to stay in equilibrium status at

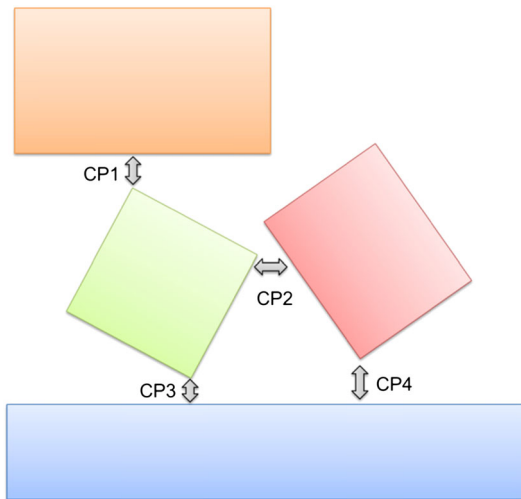


Figure 17. A system with four potential contact pair.

the end of each time step, and it needs not only to determinate the number of contact pairs among multi-bodies but also the complete convergence of imposed contact force at corresponding position in each step. Therefore, the equilibrium equations in the whole system following ‘the principle minimum potential energy’ can be established in every time step. However, the condition number of determining solution is insufficient at the beginning of the time step, even the total number of real contact pair is unknown prior to the solution of the problem, although the solution must be uniquely determined in mathematical view. The 3-D NMM method adopts the open-close iteration to solve this problem.

A simple example in Figure 17 is used to elaborate the iteration process. Assume four potential contact pair candidates, denoted by CP1, CP2, CP3 and CP4 at time instance t_n . Based on the result at time instance t_n , the real contact happens at CP1 and CP3. The penalty springs are applied immediately at these two positions. Contact status at this moment is recorded as pseudo code of ‘1010’, where ‘1’ denotes contact close and ‘0’ denotes open.

When calculating the contact solution at time instance t_{n+1} , it is initially presumed the contact status as ‘1010’. Then, we apply all other definite boundary conditions at the current time step and assemble global balance equation to gain the new position of all vertexes, indicated as I_1 . The contact detection subroutine is recalled to verify the penetration status for the known array I_1 . The result shows that the contact status changes to ‘0110’ (different from the initial value ‘1010’), which indicates an inappropriate presumption in previous iteration. The global balance equations are returned to their original formulation at time instance t_n , and the contact status is reassumed as ‘0110’, which refers to the result of last iteration. The calculation will yield a new solution I_2 . The contact detection subroutine is recalled again to have another new status of ‘1110’.

Such iteration continues until the contact status of I_n is consistent with presumed value. The contact information is recorded, and the calculation for the time step t_{n+1} is completed.

5.2. 3-D NMM flowchart

Flowchart for 3-D NMM equipped with the proposed contact algorithm is illustrated in Figure 18.

In each time step, the system equation (assemblage of inertia force matrix, displacement boundary matrix, elastic matrix, initial stress matrix, point loading matrix and volume force matrix) is constructed and solved for the unknowns. A preliminary solution is first obtained and checked to see how well the constraints are satisfied. If tension or penetration is found for any contact pair, the constraints are adjusted, and a modified system equation is formed from which a new solution is obtained. This process is repeated until no tension and no penetration are satisfied for all contact pairs. The calculation continues to the next time step.

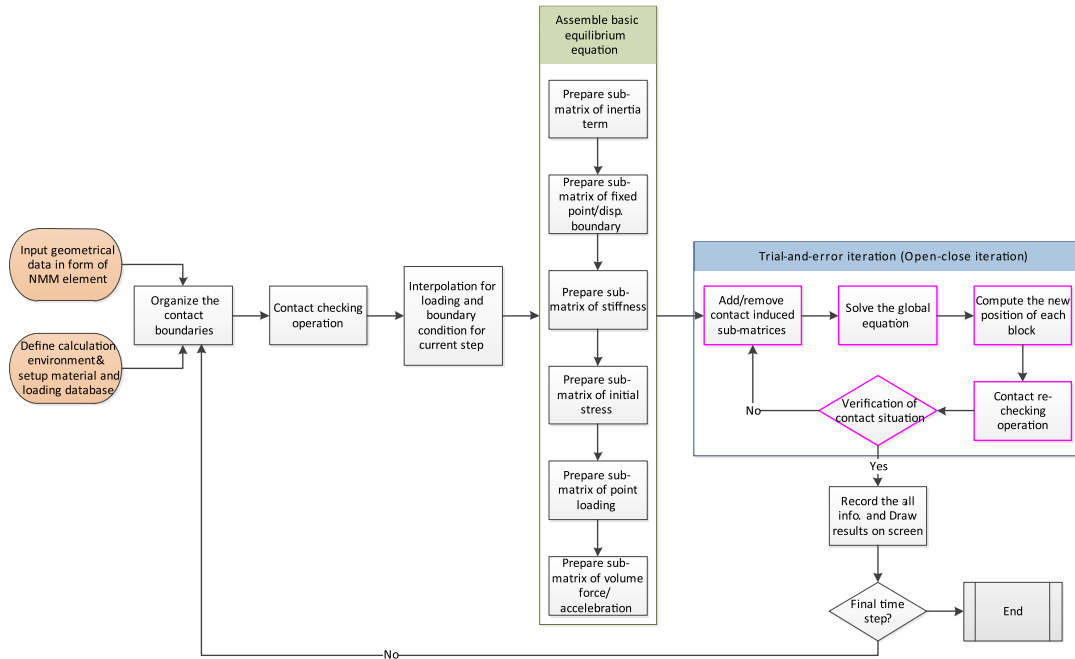


Figure 18. Flowchart of three-dimensional numerical manifold method (NMM) with contact treatment capacity.

6. CALIBRATION EXAMPLES

In this section, three examples are presented to test the accuracy and reliability of the proposed contact algorithm for the 3-D NMM. The first one is a 3-D domino run with sequential contact. The second one is collapse of a 3-D Dougong/bracket structure. The last one is collapse of kentledge.

6.1. Domino run

A typical 3-D domino run problem shown in Figure 19(a) is numerically investigated using the 3-D NMM. The numerical model consists totally 19 domino blocks with the size of $291.4 \text{ mm} \times 184.8 \text{ mm} \times 37.1 \text{ mm}$ and the approximate spacing of 239.1 mm resting on a horizontal plane. The mechanical properties are Density $\rho = 2000 \text{ kg/m}^3$, Young's modulus $E = 200 \text{ GPa}$, Poisson's ratio $\nu = 0.3$, penalty spring stiffness $k_N = k_T = 10E$, gravity acceleration $g = 10 \text{ m/s}^2$, friction angle between the domino blocks $\phi_1 = 35^\circ$, friction angle between the domino blocks and the ground $\phi_2 = 35^\circ$.

The 3-D NMM model involves 259 manifold elements with meshing size as 0.75, as shown in Figure 19(b).

In the initial state, the first block has been leaned, acting as the initial momentum in the system. The first block topples onto the second block through gravity, which induces a toppling process shown in Figure 20. The numerically obtained results are consistent with the experimentally observed phenomenon [40].

In order to check the consistency of the algorithm, one more numerical experiment is carried out. Besides the toppling of the first block under gravity with friction, an initial rotation velocity is imposed to the last block in the 3-D domino system, and it smashes itself to the second block from the last. This initial setting will produce a simultaneous toppling process from both sides of the 3-D domino system, as shown in Figure 21. The numerical result shows that the two-side simultaneous domino motion will stop at the time of 2.05 s, where the ninth block and the tenth block will lean against each other as 'Λ' shaped, consistent with the theoretical expectation.

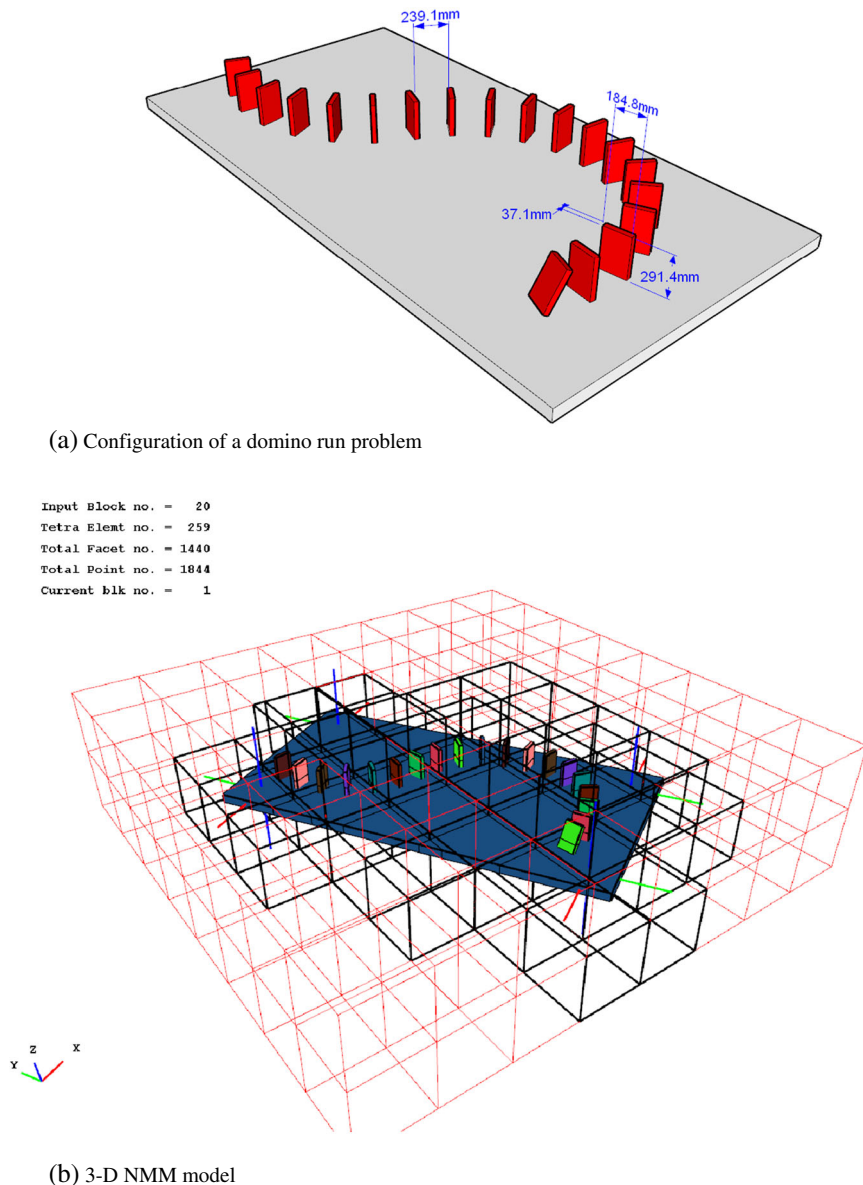


Figure 19. A three-dimensional domino run problem.

6.2. Collapse of a dougong/bracket structure

The dougong style (also known as corbel arch, Tou-Kung, a wooden bracket structure) is built up by placing crossbeam on the top of columns. This unique interlocking wooden bracket is one of the most important architecture styles in ancient China. Dougong was widely used in the Spring and Autumn Period in Chinese history (770 BC–467 BC). This architecture style is also commonly found in the modern development, for example, the China Pavilion in World Expo 2010, Shanghai. The main structure of the China Pavilion, ‘The Crown of the East’, has a distinctive roof, made of traditional dougong or brackets. The stability analysis to such dougong structure and its failure mechanism are important to production safety and also to prevent potential threat of terrorist attack.

In this example, a simplified dougong structure is studied using the 3-D NMM for its collapsing process by assuming it is subjected to pre-damage in one column. The aim is to test the consistency of crossing-lines contact mode in the 3-D contact algorithm. As shown in Figure 22, the whole

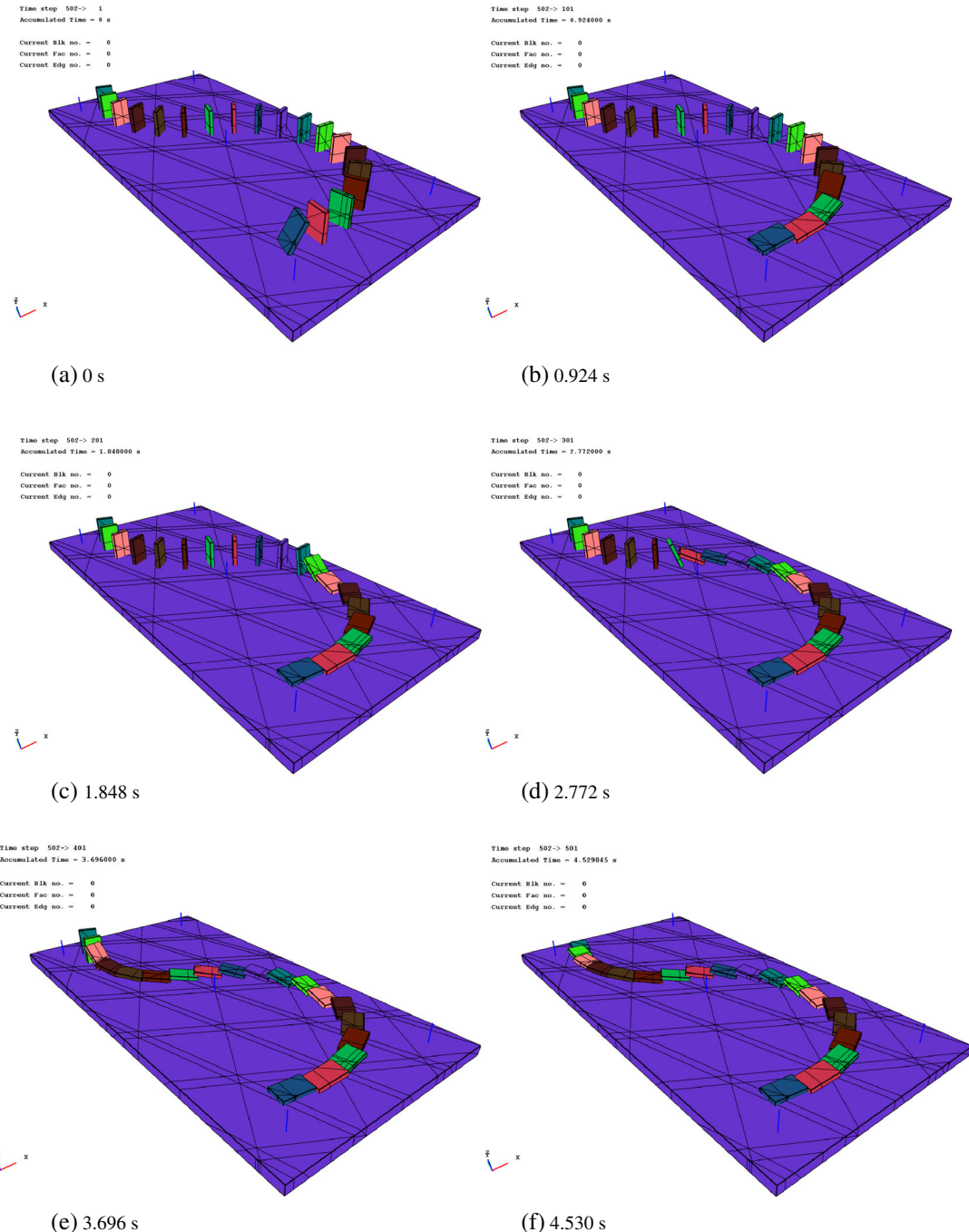


Figure 20. Domino run process modeled by three-dimensional numerical manifold method.

structure is resting on a flat plane and built up by 3 columns and 12 beams, where the 12 beams are arranged into four layers superposed to each other, as in a hexahedral pattern.

The structure is modeled with 326 manifold elements. There are totally 798 contact pairs at the end of the first time step, among them 628 contact pairs are determined to be crossing-lines mode. Total calculation runs through 500 time steps in 3.68 s. The total CPU time is about 25 min for the whole problem on a general computer with Intel E8500 and 3G RAM.

The collapse process of the structure is shown in Figure 23. Even though quantitative analysis has not been provided, qualitative studies are carried out to apply and release the contact conditions to

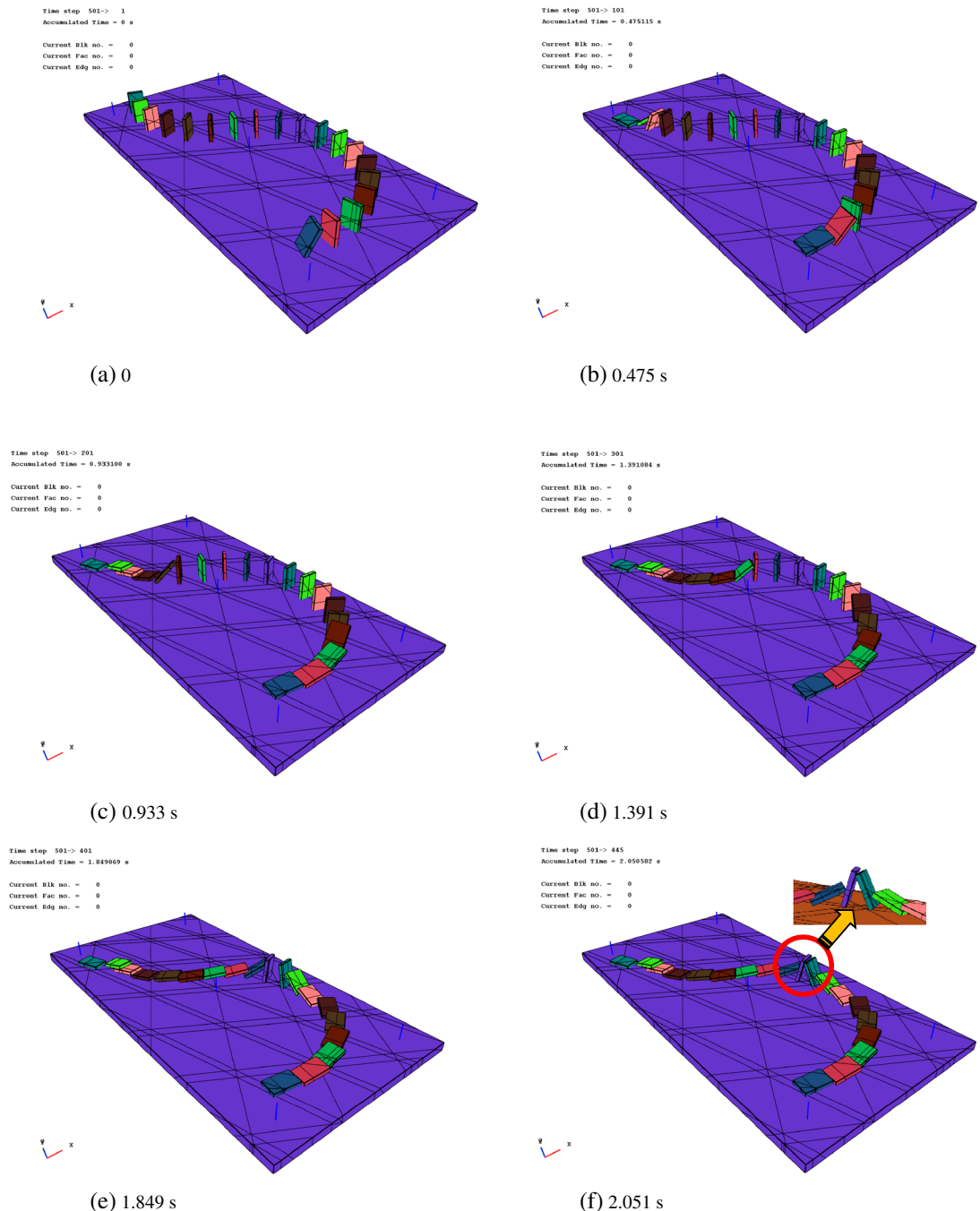


Figure 21. Two-end domino run process modeled by three-dimensional numerical manifold method.

demonstrate the phenomenon process. The whole modeling process from pre-processing to calculation results are relatively easy to operate, and the 3-D NMM shows its stability in running different cases. It has already verified and demonstrated the reliability and accuracy of the implemented contact algorithm.

6.3. Collapse of kentledge

This example is designed to investigate an accident of collapse of kentledge occurred in a construction site in Singapore.

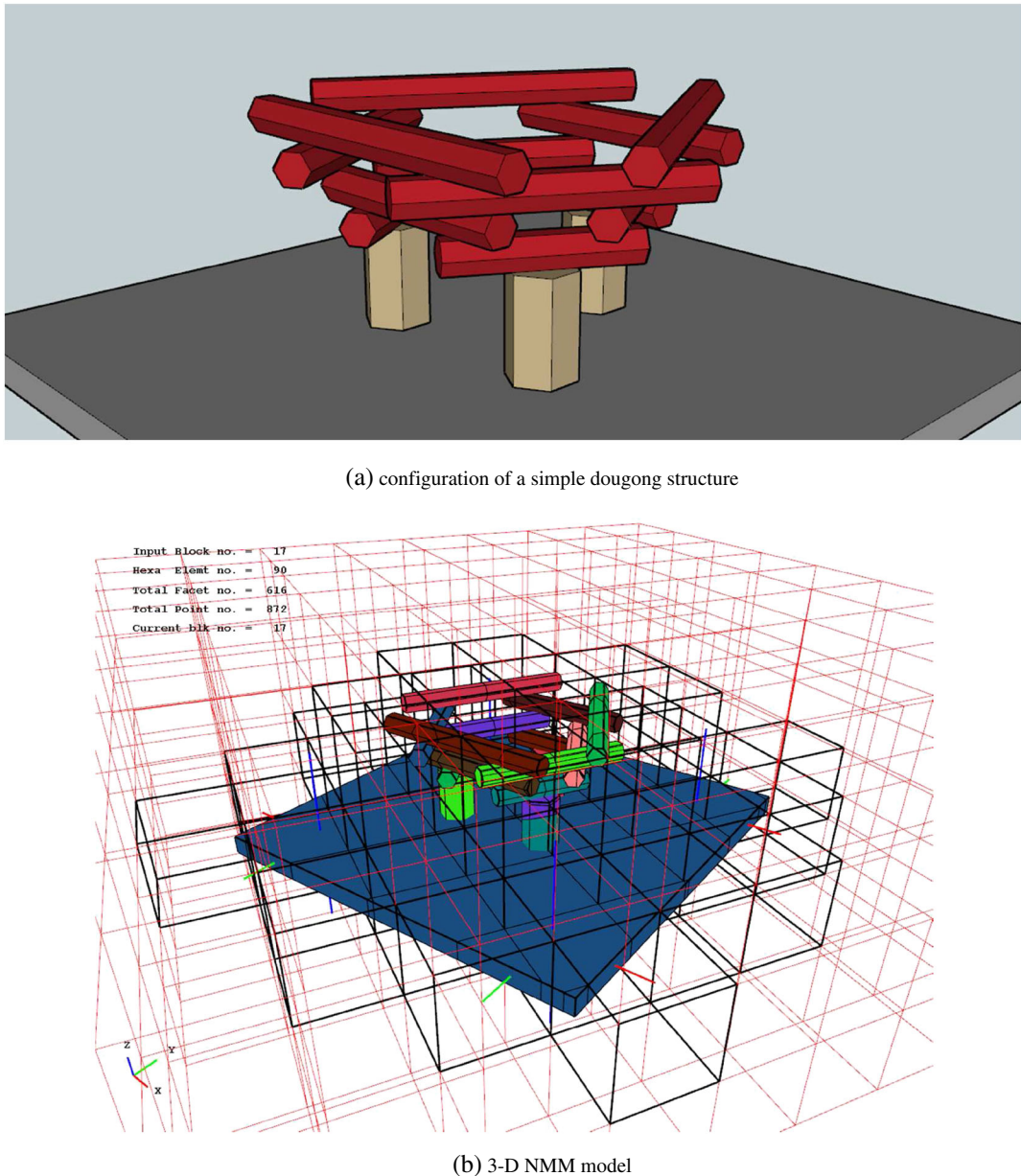


Figure 22. A dougong structure and its three-dimensional (3-D) numerical manifold method (NMM) model.

The kentledge as illustrated in Figure 24 was used to check the estimated load bearing capability of a pile on the site of an intended project. The test consists of loading a pile in increments over a certain period and measuring the displacement experienced by the test pile. Load can be applied by hydraulically jacking against a weighted box or platform, or against a girder secured by anchor piles placed in the ground outside the influence of the test pile.

The kentledge was set up to test a 1.2 m diameter bored pile to three times of working load (WL), corresponding to 22,875 kN. The test pile was designed for a WL of 7625 kN with an additional 160 kN for negative skin friction. The size of the concrete blocks used for the kentledge system is 0.8 m × 0.9 m × 1.5 m. The kentledge system remained stable for the first two cycles of tests at 1 × WL and 2 × WL. The third cycle test was carried out with additional concrete blocks to load the pile to 25,050 kN (>3 × WL). The load of 23,110 kN was reached at about 4:30 PM. At

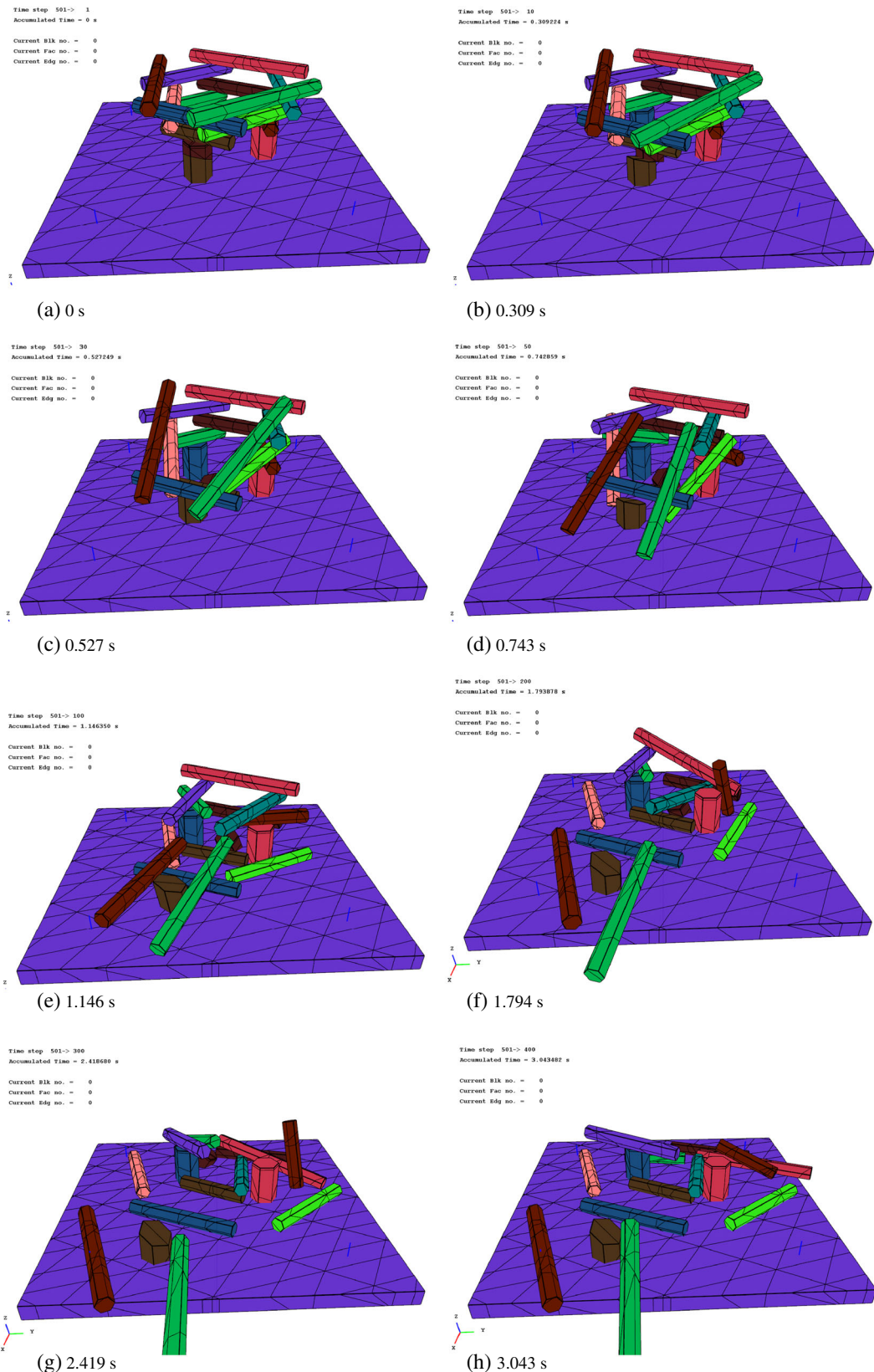


Figure 23. Collapse process of the dougong structure modeled by three-dimensional numerical manifold method.



Figure 24. An example of a kentledge.

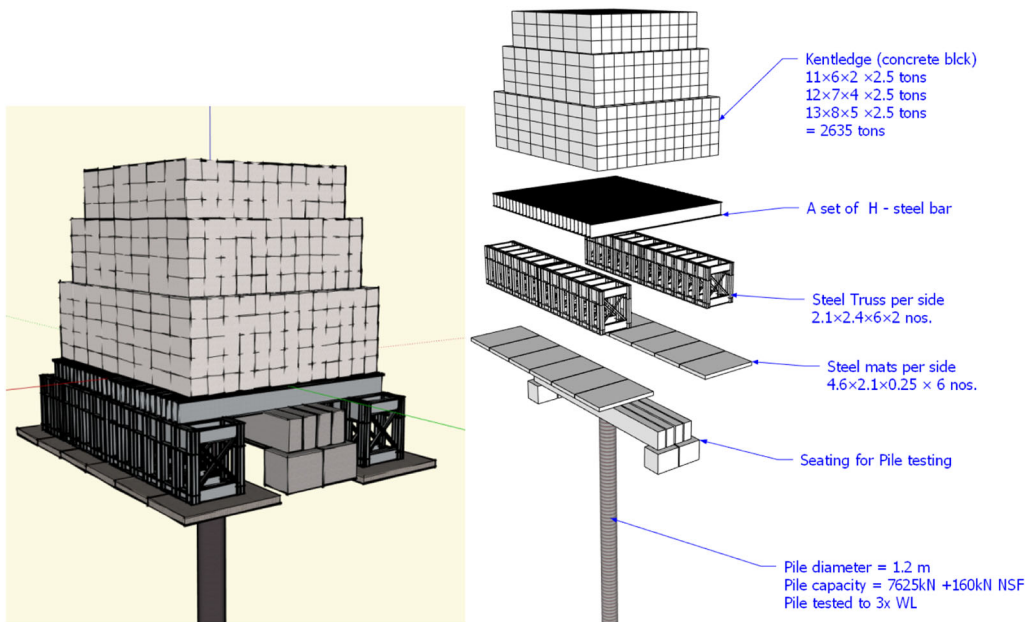


Figure 25. Kentledge setup.

Table III. Parameters used in kentledge collapse.

Item	Parameters	Value
Concrete	Unit weight (kN/m ³)	26.57
	Poisson's ratio	0.25
	Young's modulus (GPa)	24.50
Steel	Unit weight (kN/m ³)	78.70
	Poisson's ratio	0.27
	Young's modulus (GPa)	200
Interface	Initial frictional angle (°)	15.00–59.00
	Cohesion (MPa)	0.0
	Tensile strength (MPa)	0.0
Analysis parameters	Maximum displacement ratio	0.003
	Maximum time increment (s)	0.001
	Normal spring stiffness (MN/m)	320.00

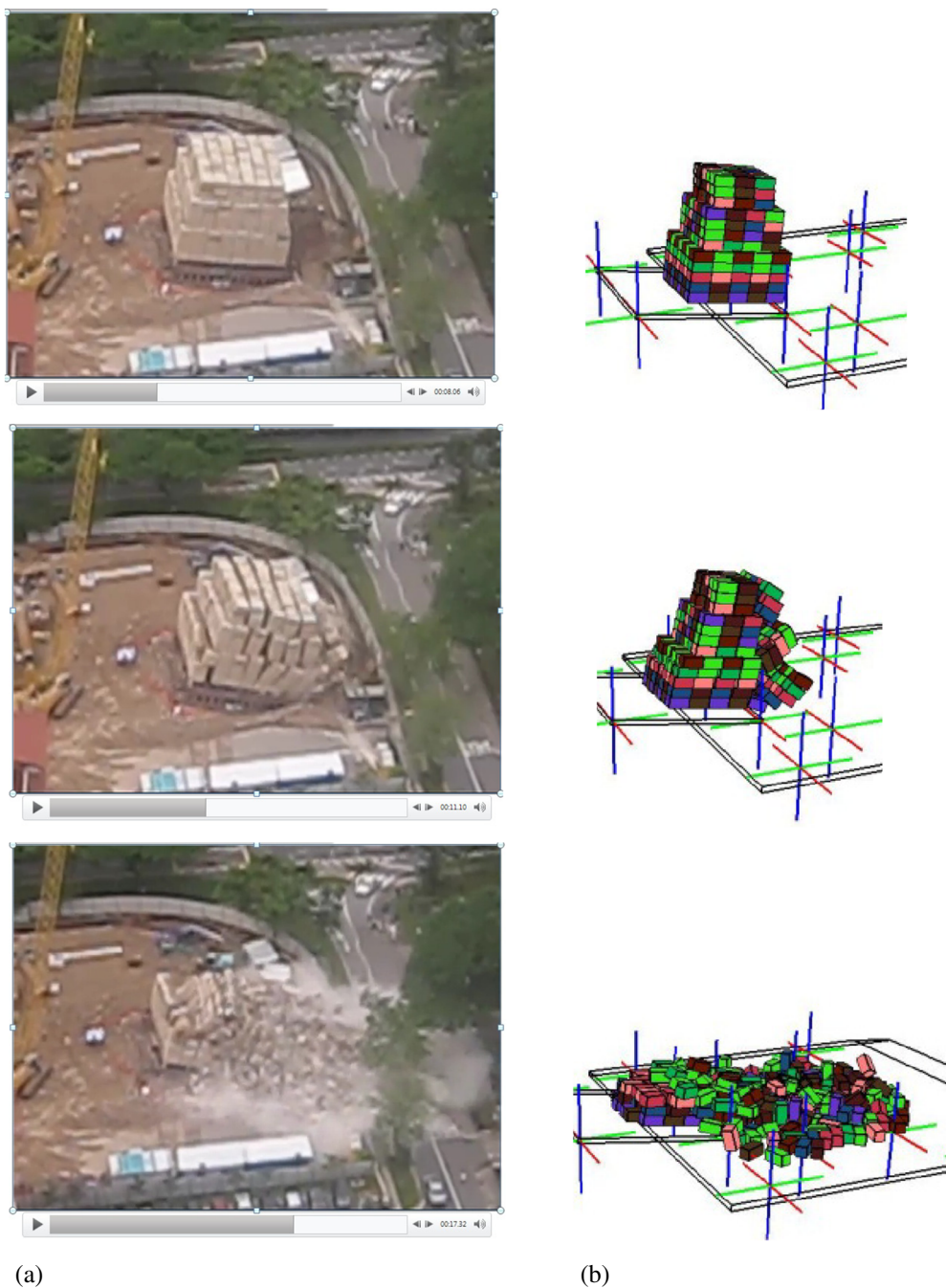


Figure 26. Comparison of collapse process of kentledge: (a) video recording at site; (b) three-dimensional numerical manifold method results.

6:10 PM, the pile shaft broke below the filled soil. Because of this failure, the pile immediately unloaded to about 4000 kN. Subsequently, the kentledge started to tilt progressively until it finally collapsed by toppling at about 8:30 AM on the next day. No visible signs of warping or damage to the steel frame were observed. Visual inspection indicated that hardcore was placed below the base of the kentledge. Signs of structural failure due to inadequate welding or structural instability were not observed. The sunken steel frame showed signs of foundation failure due to inadequate bearing capacity.

The numerical model for the kentledge is shown in Figure 25, which consists of 1056 concrete blocks. The parameters used for both the material and the calculation are listed in Table III. Based on the field observation, the following conditions are assumed: (1) concrete blocks, steel members and soil ground keep in the elastic range, no break for concrete blocks and steel supports; (2) Mohr–Coulomb constitutive model for interactions between soil and blocks as well as the interfaces among blocks; (3) linear settlement implemented; (4) no yielding or buckling for I-shaped steel bars; (5) manually settlement applied through displacement boundary; and (6) simplification on the structure (e.g., geometry of steel truss).

The 3-D NMM predicted collapse process is compared with the accident recording in Figure 26. Collapsing duration time and the collapsing range match well with the video recording.

7. CONCLUDING REMARKS

This paper proposes an efficient and reliable contact detection and enforcement algorithm to treat interactions of multiple blocks within the 3-D NMM framework. The 3-D NMM model may contain arbitrary-shaped blocks and elements, which makes the contact detection extremely complicated. The existing contact detection algorithms, which were developed under FEM or DEM framework, are not directly applicable.

A customized contact detection algorithm by extension/combination of previous algorithms is thus developed. Inspired by Zhong and Nilsson [28], a new hierarchical contact system is established in order to achieve an efficient contact detection scheme. The mathematical mesh/cells, a unique component in the NMM, is utilized for global searching of possible contact blocks and manifold elements. Local searching is followed to identify primitive hierarchies and transfers them to either one of two entrance modes: point-to-plane and crossing-lines modes. A unified formulation is derived to evaluate the penetration distance of two entrance modes and to locate real contact pairs. Penalty method is adopted to enforce the contact constraints. Mohr–Coulomb slip criterion is assumed for joints. Each contact pair has three statuses: separation, stick and slide. Normal spring, tangential spring and frictional force are applied according to the contact status. Stiffness matrices and loading vectors due to normal/tangential spring and frictional forces are derived in detail. Because of the implicit scheme framework, open-close iteration is performed within each time step to determine the correct number of contact pairs and to achieve complete convergence of imposed contact force at corresponding position.

Three benchmark problems have been conducted. The accuracy and efficiency of the proposed contact algorithm have been verified. The algorithm proposed within the 3-D NMM framework is also ready to be implemented into the 3-D DDA code.

ACKNOWLEDGEMENTS

The financial support received from the Underground Technology and Rock Engineering (UTRE) Program and the Nanyang Centre for Underground Space (NCUS), Nanyang Technological University, is acknowledged. The authors also wish to thank Dr. Genhua Shi and Prof. Guowei Ma for their valuable advice during the development of this research work.

REFERENCES

- Shi GH. Manifold method of material analysis, 1991; 57–76.
- Ma G, An X, Zhang H, Li L. Modeling complex crack problems with numerical manifold method. *International Journal of Fracture* 2009; **156**:21–35.
- Zhang H, Li L, An X, Ma G. Numerical analysis of 2-D crack propagation problems using the numerical manifold method. *Engineering Analysis with Boundary Elements* 2010; **34**:41–50.
- Terada K, Asai M, Yamagishi M. Finite cover method for linear and non-linear analyses of heterogeneous solids. *International Journal for Numerical Methods in Engineering* 2003; **58**:1321–1346.
- Mao K, Terada K. Finite cover method with multi-cover layers for the analysis of evolving discontinuities in heterogeneous media. *International Journal for Numerical Methods in Engineering* 2009; **79**(1):1–24.
- Li S, Cheng Y, Wu Y. Numerical manifold method based on the method of weighted residuals. *Computational Mechanics* 2005; **35**(6):470–480.

7. Ning Y, An X, Ma G. Footwall slope stability analysis with the numerical manifold method. *International Journal of Rock Mechanics and Mining Sciences* 2011; **48**:964–975.
8. Zhao G, Ma G, Zhang H, Zhao J. A numerical manifold method for plane micropolar elasticity. *International Journal of Computational Methods* 2010; **7**(1):151–166.
9. Zhang G, Zhao Y, Peng X. Simulation of toppling failure of rock slope by numerical manifold method. *International Journal of Computational Methods* 2010; **7**(1):167–189.
10. Wu Z, Wong L. Frictional crack initiation and propagation analysis using the numerical manifold method. *Computers and Geotechnics* 2011; **39**:38–53.
11. An X, Ma G, Cai Y, Zhu H. A new way to treat material discontinuities in the numerical manifold method. *Computer Methods in Applied Mechanics and Engineering* 2011; **200**(47–48):3296–3308.
12. Terada K, Maruyama A, Kurumatani M. Eulerian finite cover method for quasi-static equilibrium problems of hyperelastic bodies. *Communication in Numerical Methods in Engineering* 2007; **23**(12):1081–1094.
13. Shi GH. Discontinuous deformation analysis – a new numerical model for the static and dynamics of block systems,. *PhD dissertation*, Department of Civil Engineering, UC Berkeley, 1988.
14. Yeung M, Jiang Q, Sun N. Validation of block theory and three-dimensional discontinuous deformation analysis as wedge stability analysis methods. *International Journal for Rock Mechanics and Mining Science* 2003; **40**:265–275.
15. Jiang Q, Yeung M. A model of point-to-face contact for three-dimensional discontinuous deformation analysis. *Rock Mechanics and Rock Engineering* 2004; **37**(2):95–116.
16. Yeung M, Jiang Q, Sun N. A model of edge-to-edge contact for three-dimensional discontinuous deformation analysis. *Computers and Geotechnics* 2007; **34**(2):175–186.
17. Wang J, Lin G, Liu J. Static and dynamic stability analysis using 3D-DDA with incision body scheme. *Earthquake Engineering and Engineering Vibration* 2006; **5**(2):273–283.
18. Wu J, Juang C, Lin H. Vertex-to-face contact searching algorithm for three-dimensional frictionless contact problems 2005; **63**:876–897.
19. He L, Ma G. Development of 3D numerical manifold method. *International Journal of Computational Methods* 2010; **7**(1):107–129.
20. Terada K, Kurumatani M. An integrated procedure for three-dimensional structural analysis with the finite cover method. *International Journal for Numerical Methods in Engineering* 2005; **63**:2102–2123.
21. Jiang Q, Zhou C, Li D. A three-dimensional numerical manifold method based on tetrahedral meshes. *Computers & Structures* 2009; **87**:880–889.
22. Jiang Q, Deng S, Zhou C, Lu W. Modeling unconfined seepage flow using three-dimensional numerical manifold method. *Journal of hydrodynamics* 2010; **22**(4):554–561.
23. Cheng YM, Zhang YH. Formulation of a three-dimensional numerical manifold method with tetrahedron and hexahedron elements. *Rock Mechanics and Rock Engineering* 2008; **41**(4):601–628.
24. Williams JR, O'Connor R. A linear complexity intersection algorithm for discrete element simulation of arbitrary geometries. *Engineering Computations* 1995; **12**(2):185–201.
25. Bonnet J, Peraire J. An alternating digital tree (ADT) algorithm for 3D geometric searching and intersection problem. *International Journal for Numerical Methods in Engineering* 1991; **31**:1–17.
26. Perkins E, Williams JR. A fast contact detection algorithm insensitive to object size. *Engineering Computations* 2001; **18**(1–2):48–61.
27. Munjiza A, Andrews KRF. NBS contact detection algorithm for bodies of similar size. *International Journal for Numerical Methods in Engineering* 1998; **43**(1):131–49.
28. Zhong ZH, Nilsson L. A unified contact algorithms based on the territory concept. *Computer Method in Applied Mechanics and Engineering* 1996; **130**:1–16.
29. Belytschko T, Yeh IS. The splitting pinball method for contact-impact problems. *Computer Method in Applied Mechanics and Engineering* 1993; **105**:375–393.
30. Wang SP, Nakamachi E. The inside-outside contact search algorithm. *International Journal for Numerical Methods in Engineering* 1997; **40**:3665–3685.
31. Cundall PA. Formulation of three-dimensional Distinct Element Model-part I: a scheme to detect and represent contacts in a system composed of many polyhedral blocks. *International Journal of Rock Mechanics and Mining Sciences and Geomechanics Abstracts* 1988; **25**(3):107–116.
32. Chen WS, Zheng H, Cheng YM, Ge XR. Detection of 3D rock block contacts by penetration edges. *Chinese Journal of Rock Mechanics and Engineering* 2004; **23**(4):565–571.
33. Ahn TY, Song JJ. New contact-definition algorithm using inscribed spheres for 3D discontinuous deformation analysis. *International Journal of Computational Methods* 2010; **8**(2):171–191.
34. Lin CT, Amadei B, Jung J, Dwyer J. Extensions of discontinuous deformation analysis for jointed rock masses. *International Journal of Rock Mechanics and Mining Sciences and Geomechanics Abstracts* 1996; **33**(7):671–694.
35. Wriggers P. *Computational Contact Mechanics*. John Wiley & Sons: Chichester, 2002.
36. Bazaraa MS, Sherali HD, Shetty CM. *Nonlinear Programming: Theory and Algorithms*, 2nd ed. John Wiley & Sons: New York, 1993.
37. Zavarise G, Wriggers P. On contact between three-dimensional beams undergoing large deflections. *Communications in numerical methods in engineering* 1997; **13**:429–438.
38. Goodman RE, Shi GH. *Block Theory and Its Application to Rock Engineering*. Prentice-Hall: Englewood Cliffs, NJ, 1985.

39. Shi GH. Simplex integration for manifold method, FEM, DDA and analytical analysis. *Proceeding of first International Forum on Discontinuous Deformation Analysis (DDA) and Simulations of Discontinuous Media*, TSI Press, Albuquerque, NM, Mexico, 1996; 205–262.
40. Bates B. Development and DDA modeling of benchmark tests. *B.S.c. Thesis*, Department of Civil and Engineering, University of Cape Town, South Africa, 2004.